1   Radiative Forcing by Light-Absorbing Particles in Snow in Northeastern China

2   Retrieved from Satellite Observations

3   Wei Pu[1], Jiecan Cui[1], Tenglong Shi[1], Xuelei Zhang[2], Cenlin He[3], and Xin Wang[1]

5   [1]Key Laboratory for Semi-Arid Climate Change of the Ministry of Education, College

6   of Atmospheric Sciences, Lanzhou University, Lanzhou 730000, China

7   [2]Key Laboratory of Wetland Ecology and Environment, Northeast Institute of

8   Geography and Agroecology, Chinese Academy of Sciences, Changchun 130102,

9   China

10   [3]National Center for Atmospheric Research, Boulder, CO 80301, USA

12   Corresponding author: Xin Wang (wxin@lzu.edu.cn)

1 **Abstract.** Light-absorbing particles (LAPs) deposited on snow can decrease snow

2 albedo and affect climate through the snow-albedo radiative forcing. In this study, we

3 use MODIS observations combined with a snow albedo model (SNICAR) and a

4 radiative transfer model (SBDART) to retrieve the radiative forcing by LAPs in snow

5 (RF_{MODIS}^{LAPs}) across Northeastern China (NEC) in January-February from 2003 to 2017.

6 RF_{MODIS}^{LAPs} presents distinct spatial variability, with the minimum (22.3 W m^{-2}) in western

7 NEC and the maximum (64.6 W m^{-2}) near industrial areas in central NEC. The regional

8 mean RF_{MODIS}^{LAPs} is ~45.1±6.8 W m^{-2} in NEC. The positive (negative) uncertainties of

9 retrieved RF_{MODIS}^{LAPs} due to atmospheric correction range from 14% to 57% (-14% to -

10 47%) and the uncertainty value basically decreased with the increased RF_{MODIS}^{LAPs}. We

11 attribute the variations of radiative forcing based on remote sensing and find that the

12 spatial variance of RF_{MODIS}^{LAPs} in NEC is 74.6% due to LAPs, while 21.2% and 4.2% due

13 to snow grain size, and solar zenith angle. Furthermore, based on multiple linear

14 regression, the BC dry and wet deposition and snowfall could totally explain 81% of

15 the spatial variance of LAP contents, which confirms the reasonability of the spatial

16 patterns of retrieved RF_{MODIS}^{LAPs} in NEC. We validate RF_{MODIS}^{LAPs} using in situ radiative

17 forcing estimates. We find that the biases in RF_{MODIS}^{LAPs} are negatively correlated with

18 LAP concentrations and range from ~5% to ~350% in NEC.

1 1. Introduction

2 Pure snow is the most strongly reflective natural substance at the surface of the Earth,

3 and seasonal snow covers more than 30% of the Earth's land area (Painter et al., 1998).

4 Therefore, snow cover has an important impact on the radiation balance of the Earth

5 (Cohen and Rind, 1991). When light-absorbing particles (LAPs), such as black carbon

6 (BC), organic carbon (OC), and mineral dust deposited on snow, can effectively reduce

7 snow albedo (Hadley and Kirchstetter, 2012; He et al., 2017, 2018; Li et al., 2016;

8 Warren, 1982, 1984; Warren and Wiscombe, 1980) and enhance the absorption of solar

9 radiation (Dang et al., 2017; Kaspari et al., 2014; Liou et al., 2011, 2014; Painter et al.,

10 2012b). Warren and Wiscombe (1980) indicated out that 10 ng g^{-1} BC in old snow could

11 reduce the snow albedo by nearly 1% at 400 nm with the snow grain size of 1000 μm.

12 Based on model simulation, Jacobson (2004) pointed out that the snow albedo reduction

13 caused by BC in snow and ice is 4% in the global and 1% in the Northern Hemisphere.

14 LAPs in snow further contribute to alterations in snow morphology, accelerations in

15 snowmelt, and reductions in snow cover (Flanner et al., 2007, 2009; Painter et al., 2013a;

16 Xu et al., 2009). For example, Qian et al. (2009) simulated the deposition of BC on

17 snow and its impact on snowpack and the hydrological cycle in the western United

18 States and the results showed that BC-induced snow albedo perturbations caused a

19 decrease of snow water equivalent by 2-50 mm over the mountains during late winter

20 to early spring.

21 Several studies have estimated the radiative forcing by LAPs in snow based on model

22 simulations, which has nonnegligible effects on local hydrological cycles (Painter et al.,

1 2010; Qian et al., 2009; Yasunari et al., 2010) and regional and global climate (Bond et

2 al., 2013; Hansen and Nazarenko, 2004; He et al., 2014; Jacobson, 2002, 2004;

3 McConnell et al., 2007; Ramanathan and Carmichael, 2008; Yasunari et al., 2015). For

4 example, in the Northern Hemisphere, Hansen and Nazarenko (2004) pointed out that

5 the radiative forcing of BC on snow and ice albedo is +0.3 W m^{-2}. In addition, the

6 IPCC's AR5 (2013) indicated that the impact of BC in snow and ice accounted for a

7 global mean climate forcing of +0.04 W m^{-2}, but the confidence level is low. Bond et

8 al. (2013) estimated the climate forcing consisting of radiative forcing, rapid

9 adjustments, and the strong snow-albedo feedback due to BC-in-snow forcing and

10 pointed that the best valuation of the climate forcing by BC in snow and sea ice is +0.13

11 W m^{-2}, although the 90% uncertainty bounds are from +0.04 W m^{-2} to +0.33 W m^{-2}.

12 Nevertheless, recent studies reported that ample factors confuse the model simulation

13 of BC-in-snow induced climate forcing, and the model-based estimate of the regional

14 and global radiative forcing caused by BC in snow and ice is still a challenge (Hansen

15 and Nazarenko, 2004; Bond et al., 2013; Pu et al., 2017).

16 Much of northeastern China (NEC) is covered by contiguous seasonal snow in the

17 winter and early spring. Local pollutant emissions in this region are some of the most

18 intense in the world (Bond et al., 2004), leading to considerable amounts of LAPs

19 deposited on snow (Bond et al., 2013). Several field campaigns have been conducted

20 to analyze LAPs concentrations in snow across NEC (Huang et al., 2011; Wang et al.,

21 2014a, 2015). Wang et al. (2013) conducted a large field campaign to measure LAPs in

22 seasonal snow in northern China from January to February 2010. They found that BC

1   is the dominant absorber compared with OC and dust in NEC and BC concentrations

2   in snow in this region range from 40 ng g^{-1} to 4000 ng g^{-1}, which are much higher than

3   those measured in the Arctic, North America and Europe (Doherty et al., 2010, 2014;

4   Peltoniemi et al., 2015). Recently, Wang et al. (2017) compared measured and

5   simulated snow albedos and showed that LAPs can reduce the visible spectral albedo

6   in NEC to 0.65, which indicated a significant impact of LAPs on snow albedo reduction.

7   Zhao et al. (2014) simulated the radiative forcing by LAPs in snow over northern China

8   using a coupled model; however, they noted that the uncertainties of their results are

9   non-negligible, due to the limited observations that are available.

10   Remote sensing is considered to be a powerful tool for estimating snow physical

11   properties (e.g., Nolin and Dozier, 1993, 2000) and LAPs-induced snow albedo

12   reduction, which can provide valuable observational information for modeling studies

13   to reduce modeling uncertainties. For instance, to estimate the influence of mineral dust

14   on snow albedo in the European Alps, Di Mauro et al. (2015) defined a new spectral

15   index, the Snow Darkening Index based on in situ measured snow spectral reflectance

16   and the Landsat 8 Operational Land Imager (OLI) data, they found that the Snow

17   Darkening Index could effectively track the content of mineral dust in snow. In addition,

18   Di Mauro et al. (2017) characterized the impact of LAPs on ice and snow albedo of the

19   Vadret da Morteratsch, a large valley glacier in the Swiss Alps using satellite (EO-1

20   Hyperion) hyperspectral data. The results showed that the spatial distribution of both

21   narrow-band and broad-band indices retrieved from Hyperion was related to ice and

22   snow impurities. In the Arctic, Dumont et al. (2014) developed an Impurity Index based

1   on satellite observations (MODIS C5 surface reflectance) to analyze the snow

2   darkening caused by the increased contents of LAPs in snow in Greenland.

3   Nevertheless, Polashenski et al. (2015) pointed out that the apparent snow albedo

4   decline in Greenland observed from MODIS C5 surface reflectance (Dumont et al.,

5   2014) has a significant contribution from the uncorrected Terra sensor degradation. In

6   this study, in order to prevent the interference from the sensor degradation, we used the

7   latest version (version 6, C6) of MODIS data from Aqua sensor, which was verified to

8   not suffer from the influence of sensor degradation (Polashenski et al., 2015). Even

9   though these studies have confirmed the ability of remote sensing on assess the role of

10   LAPs in snow on snow albedo reduction, however, they didn't quantitatively estimate

11   the radiative forcing caused by LAPs in snow, which is extremely important for

12   implying the impact of LAPs on regional and global climate. Recently, Painter et al.

13   (2012a) have successfully used the MODIS Dust Radiative Forcing in Snow

14   (MODDRFS) model to retrieve surface radiative forcing by LAPs in snow cover from

15   Moderate Resolution Imaging Spectroradiometer (MODIS) surface reflectance data.

16   They found that the instantaneous at-surface radiative forcing can beyond 250 W m^{-2}

17   in the Hindu Kush-Himalaya area and falls in a range of 30-250 W m^{-2} in the Upper

18   Colorado River Basin. Painter et al. (2013b) also provided and validated an algorithm

19   suite to quantitatively retrieve radiative forcing by LAPs in snow from Airborne

20   Visible/Infrared Imaging Spectrometer (AVIRIS) data in the Senator Beck Basin Study

21   Area (SBBSA), SW Colorado, USA. The lowest radiative forcing was found on the

22   high north facing slopes while the highest on southeast facing slopes at the lowest

1   elevations. Seidel et al. (2016) analyzed the spatial and temporal distribution of

2   radiative forcing by LAPs in snow in the Sierra Nevada and Rocky Mountain from

3   imaging spectroscopy. Their results presented an increased radiative forcing from 20

4   W m^{-2} up to 200 W m^{-2} in the melting period. However, to date, no studies have

5   quantitatively attributed the contributions of each factor to the variations of radiative

6   forcing by LAPs in snow based on remote sensing. Moreover, no studies have estimated

7   the radiative forcing by LAPs in snow across NEC using remote sensing, even though

8   the LAP content is much higher compared with those in Arctic, Europe and USA (Dang

9   et al., 2017).

10   In this study, we attempt to retrieve the radiative forcing by LAPs in snow across NEC

11   using MODIS datasets combined with the Snow, Ice, and Aerosol Radiation (SNICAR)

12   model (Flanner et al., 2007, 2009) and the Santa Barbara DISORT Atmospheric

13   Radiative Transfer (SBDART) model (Ricchiazzi et al., 1998), and estimate the

14   uncertainties of radiative forcing from atmospheric correction and qualify the fractional

15   contribution of each factor to the spatial variance of RF_{MODIS}^{LAPs}. Then, we will investigate

16   the reasonability of the spatial patterns of retrieved radiative forcing in NEC based on

17   BC deposition and snowfall data. Finally, we quantitatively estimate the biases of

18   MODIS retrieved radiative forcing using in situ radiative forcing estimates, which are

19   based on field measurements.

20   2. Datasets

21   2.1. Remote Sensing Datasets

22   The latest version (Collection 6) of MODIS surface reflectance data (MYD09GA),

1 MODIS snow cover data (MYD10A1), and MODIS aerosol optical depth (AOD) data

2 (MYD04) are used in this study from 2003 to 2017 that cover the months of January

3 through February (https://modis.gsfc.nasa.gov/). The MOD09 product is divided into 7

4 bands (band 1, 620-670 nm; band 2, 841-876 nm; band 3, 459-479 nm; band 4, 545-

5 565 nm; band 5, 1230-1250 nm; band 6, 1628-1652 nm; and band 7, 2105-2155 nm),

6 and has a spatial resolution of 500 m (Vermote, 2015). The MOD09 surface reflectance

7 is an estimate of the surface spectral reflectance for each band as it would have been

8 measured at ground level as if there were no atmospheric scattering or absorption. It

9 corrects for the effects of atmospheric gases and aerosols. The performance of the

10 atmospheric correction algorithm suffers from the influence of view and solar zenith

11 angles and aerosol optical thickness; the accuracy of the algorithm is also affected by

12 the wavelengths of different bands. More details about the data product information and

13 band quality description of MOD09GA could be found in the MODIS Surface

14 Reflectance User's Guide (https://modis.gsfc.nasa.gov/data/dataprod/mod09.php).

15 MODIS satellite data has been widely accepted in retrieval of snow cover and its

16 physical properties. (e.g. Scambos et al., 2007; Rittger et al., 2013). In addition, MODIS

17 has three bands located in the visible bands (VIS) and radiometric range in the VIS over

18 snow surface has no saturation phenomenon, which provide the ability of detecting the

19 changes of reflectance in the VIS caused by LAPs in snow (Painter et al., 2012a).

20 2.2. Surface Measurement Datasets

21 Wang et al. (2017) conducted a snow survey across NEC in January 2014. They

22 measured AOD using a Microtops II Sun photometer. The Microtops II Sun photometer

1 is a portable instrument and measures solar radiance in five spectral wave bands (340,

2 440, 675, 870, and 936 nm) from which it automatically derives aerosol optical depth

3 (AOD). When the Microtops II Sun photometer is well cleaned and well calibrated, its

4 AOD retrievals can be comparable with those of CIMEL Sun photometers used in the

5 AERONET network, with uncertainties ranging from 0.01 to 0.02 (Ichoku et al., 2002).

6 The snow albedo and surface solar irradiance were measured using an Analytical

7 Spectral Devices (ASD) spectroradiometer. The Analytical Spectral Devices Inc. (ASD)

8 spectroradiometer has 3 nm spectral resolution on the visible/near infrared detector

9 (350–1050 nm, silicon photodiode array), and 10–12 nm resolution on the short wave

10 infrared detectors (900–2500 nm, InGaAs). Measurements are made by standing

11 "down-sun" of the receptor, taking consecutive scans of downwelling and upwelling

12 radiation. Wuttke et al. (2006) indicated that the ASD spectroradiometer is considered

13 as the most mobile, capable, and rapid for measuring spectral albedo during short time

14 periods, especially in very cold regions. The cosine error is less than 5% for solar zenith

15 angles below 85º at a wavelength of 320 nm. We use these datasets to validate the snow

16 grain size retrievals and the simulated surface solar irradiance values.

17 Snow samples were collected at 46 sites in January and February 2010 across Northern

18 China (Wang et al., 2013) and at 13 sites in January 2014 across Northeastern China

19 (Wang et al., 2017). A detailed description of the procedures of snow collection and

20 filtration has been presented by previous studies (Doherty et al., 2010, 2014; Wang et

21 al., 2013). Briefly, in order to keep the collected snow samples to be regionally

22 representative and minimize the influence from the local emission sources, sample

1   locations were usually chosen at least 1 km upwind away from the approach roads and

2   railways and more than 50 km from cities and towns. In addition, efforts were made to

3   collect samples in open areas in order to prevent the contaminations from the detritus

4   of bushes and trees. Generally, snow samples were collected within a vertical resolution

5   varied from ~2 cm to 10 cm and usually at typically vertical intervals of 5 cm from the

6   top to the bottom throughout the snowpack depth at each site. In a case of a visibly

7   distinct layering, such as newly fallen snow at surface layer or a melt layer, the snow at

8   that layer was gathered individually. Right and left snow samples of two side-by-side

9   vertical profiles were collected within each layer to make a comparison and average the

10   snow sample pairs. All snow samples were maintained frozen to prevent the melting

11   snow from influencing the LAPs content. Usually every 3 to 4 days, snow samples were

12   filtered at temporary laboratories set up in hotels. Simply, snow samples were melted

13   and filtered through Nuclepore filters of 0.4 μm pore size. The samples of "before" and

14   "after" filtration were gathered and refrozen for the following chemical analysis, and

15   the filters were used for optical analysis.

16   An integrating sphere/integrating sandwich spectrophotometer (ISSW) was applied to

17   analyze the filters and quantify the spectral light absorption by LAPs in snow. ISSW

18   was firstly described by Grenfell et al. (2011), modified by Wang et al. (2013) and

19   Doherty et al. (2014), and has been used by some previous studies (Dang and Hegg,

20   2014; 2014; Pu et al., 2017; Zhou et al., 2017). Schwarz et al. (2012) has confirmed the

21   performance of ISSW in quantifying LAPs concentrations in snow by comparing with

22   the Single Particle Soot Photometer (SP2) although both SP2 and ISSW may suffer

1 from non-negligible uncertainties. Briefly, ISSW produces a diffuse radiation field

2 when white light illumination is transmitted into an integrating sphere, then the diffuse

3 radiation pass through the filter from below and is measured by a spectrometer. By

4 measuring a sample filter and a blank filter, respectively, ISSW acquires the light

5 attenuation spectrum due to the loadings on sample filter (Grenfell et al., 2011).

6 Because of the design that the measured filter is sandwiched between two integrating

7 spheres, the light attenuation is nominally due to the absorption of LAPs on the filter

8 and the influence of light scattering is negligible (Doherty et al., 2014). ISSW measures

9 the light attenuation from 400 nm to 700 nm benefited from the optimal signal-to-noise

10 ratio, and then extends the full spectral to a range of 350 to 750 nm by extrapolation

11 (Pu et al., 2017). Calibration is done by measuring a set of fullerene (a synthetic BC,

12 Alfa Aesar, Inc., Ward Hill, MA, USA) filters with a range of known loadings. Then,

13 the light attenuation spectrum of the sample filter is transformed to an equivalent BC

14 mass loading by against the standard filters. With the loaded area on the filter and the

15 volume of filtered snow water, equivalent BC mass is converted to equivalent BC

16 concentration (BC_{equiv}). In this study, we will use BC_{equiv} on behalf of all LAPs to

17 calculate the in situ radiative forcing.

18 2.3. BC Deposition and Snowfall Data

19 BC deposition and snowfall both have important effects on the radiative forcing by

20 LAPs in snow (Seidel et al., 2016). Higher BC deposition indicates that greater amounts

21 of BC are deposited on snow, reducing the snow albedo. A higher frequency of snowfall

22 implies that greater amounts of fresh snow, which has smaller snow grains than aged

1   snow, are present at the surface, increasing the snow albedo (Wang et al., 2014b).

2   Therefore, we examine the retrieved results based on the snowfall data in January-

3   February from 2003 to 2017 from the ERA-Interim reanalysis

4   (http://apps.ecmwf.int/datasets/data/interim-full-daily/levtype=sfc/), and the BC dry

5   and wet deposition data of MIROC5 historical experiments from phase 5 of the Coupled

6   Model Intercomparison Project in January-February from 2003 to 2005 (CMIP5;

7   Taylor et al., 2012).

8   3. Methods

9   3.1. Models

10   3.1.1. SNICAR model

11   Snow, Ice, and Aerosol Radiative (SNICAR) model is the most widely used multi-layer

12   snow albedo model in the fields of atmospheric sciences. Flanner et al. (2007) has

13   presented a comprehensive description for SNICAR model. Here, we just briefly give

14   a summary of SNICAR. SNICAR simulates radiative transfer in snowpack based on

15   the theory of Wiscombe and Warren (1980) and the two-stream multilayer radiative

16   approximation of Toon et al (1989). The input optical parameters (mass extinction

17   coefficient, single scatter albedo, and asymmetry factors) of snow grains and LAPs are

18   off-line calculated using Mie theory. In addition, the types of surface spectral

19   distribution (clear- or cloudy-sky) and incident radiation (direct or diffuse) can be

20   chosed by users, and users must specify the solar zenith angle if the incident flux is

21   direct. In general, users should input the parameters involving the type of surface

22   spectral distribution and incident radiation, number of snow layers, snow thickness,

1 density, snow grain radius, and the type and concentration of LAPs in each snow layer,

2 the albedo of underlying ground, Following the previous study (Painter et al., 2012a),

3 we assume one-layer semi-infinite snow to drive SNICAR model in this study.

4 3.1.2. SBDART model

5 In this study, we use the Santa Barbara DISORT Atmospheric Radiative Transfer

6 (SBDART) model (Ricchiazzi et al., 1998) to simulate the surface solar irradiance.

7 SBDART is one of the most widely used models to calculate the radiative transfer at

8 the Earth's surface and within the atmosphere in both clear and cloudy sky. SBDART

9 is a combination of a DISORT (Discrete Ordinate Radiative Transfer) radiative transfer

10 module (Stamnes et al., 1988), low-resolution atmospheric transmission models, and

11 Mie theory. The radiative transfer equations for a plane-parallel, vertically

12 inhomogeneous, non-isothermal atmosphere numerically integrated in SBDART are

13 based on DISORT and light scattering by water droplets and ice crystals results from

14 Mie theory. SBDART already considers all important processes that affect the

15 ultraviolet, visible, and infrared radiation fields. The key components of SBDART

16 include standard atmospheric models, cloud models, extraterrestrial source spectra, gas

17 absorption models, standard aerosol models, and surface models. SBDART is well

18 suitable for a widespread use in atmospheric radiation and remote sensing studies. More

19 details about SBDART model could be found in the paper of Stamnes et al. (1988).

20 3.2. Retrieval Methods

21 In this study we use BC as a representative to describe the effect of LAPs on snow

22 albedo. Figure 1a shows the spectral snow albedo from 300 to 1400 nm. Gray areas

1   show the typical spectral solar irradiance at the time of MODIS Aqua overpass (local

2   time of 1:30 PM) in January-February of NEC; the yellow column bars represent

3   MODIS bandpasses. We can see that when LAPs such as BC deposited on snow, can

4   effectively reduce snow albedo in the visible bands, which contain about half of total

5   solar radiation. For a snowpack with snow grains radius of 100-300 μm, 100 ng g^{-1} BC

6   in snow (a typical BC concentration in snow of the remote clean areas in NEC) can

7   reduce snow albedo of ~0.05-0.08 at 500 nm; 1000 ng g^{-1} BC in snow (a typical BC

8   concentration in snow of the polluted industrial areas in NEC) can reduce snow albedo

9   of ~0.12-0.2. On the other hand, the effects of BC decrease at longer wavelengths in

10   the near infrared (NIR). Moreover, when wavelengths exceed 1150 nm, snow albedo is

11   dominated by the snow optical effective radius (R_{eff}) and is independent of LAPs. As

12   shown in Figure 1b, snow albedo reduction is not only dependent on LAPs in snow but

13   also snow grains size and solar zenith angle (θ). Generally, the reduction in snow albedo

14   caused by BC increases with BC concentration and R_{eff}, whereas it decreases with the

15   solar zenith angle (θ). Based on these characteristics, we retrieve R_{eff}, the reduction in

16   snow albedo, and the radiative forcing by LAPs in this section.

17   3.2.1. Snow Cover

18   Three methods have been widely used in mapping snow-covered area using MODIS

19   data. In the first method, "binary" maps, pixels are classified as either "snow-free" or

20   "snow-covered" (Hall et al., 1995). However, significant errors exist in such maps, as

21   pixels with a resolution of 500 m are not always completely covered by snow. The

22   second method, the MODSCAG retrieval algorithm, is a fractional snow algorithm that

1   is based on spectral mixture analysis (Painter et al., 2009). However, it cannot be

2   applied in NEC, due to limited information on the spectral reflectances of the vegetation,

3   soils and rock in this region. Therefore, we use the third method, which is based on the

4   reflectances in the visible bands and the normalized difference snow index (NDSI):

5   $$\text{NDSI}=\frac{R_{band4}-R_{band6}}{R_{band4}+R_{band6}} \qquad (1)$$

6   where R_{band4} and R_{band6} are the surface reflectances in bands 4 and 6. Following Negi

7   and Kokhanovsky (2011), an area is determined to be snow-covered if the NDSI and

8   the reflectance in band 4 both exceed 0.6. We note that the following analysis are only

9   done over the defined snow covered areas and periods.

10   3.2.2. Retrieval of Snow Grain Size

11   Many methods have been used to retrieve snow grain size (e.g., Lyapustin et al., 2009;

12   Nolin and Dozier, 1993). However, in NEC, the efficacy of most of these methods is

13   limited, as the reflectances in bands 1-4 are seriously affected by LAPs in polluted snow

14   (Figure 1a), and the reflectances in bands 6-7 are not sensitive to R_{eff}. Hence, R_{eff} is

15   retrieved at a wavelength of 1240 nm (the central wavelength of band 5) using SNICAR

16   (Wang et al., 2017).

17   We validate the retrieved R_{eff} values using in situ measurements. The mean absolute

18   error (MAE) is 71 μm, which is slightly higher than that reported by Painter et al. (2009).

19   Nevertheless, the results are still credible because this study investigates a larger spatial

20   scale than the previous study.

21   3.2.3. Impurity Index

22   To assess LAP contents in snow, we use the surface reflectances in bands 4-5 to derive

1 an impurity index (I_{LAPs}):

2 $$I_{LAPs} = \frac{\ln(R_{band4})}{\ln(R_{band5})} \tag{2}$$

3 This quantity increases with the LAP content but is almost independent of R_{eff} and θ

4 (Figure 1c). Di Mauro et al. (2017) has successfully exhibited I_{LAPs} to assess the

5 variations of LAP contents in the snow of the Morteratsch Glacier in the Swiss Alps.

6 In this study, we didn't retrieve the concentrations of LAPs. Because such retrieval is

7 constrained by many unknown factors, such as size distribution, optical properties and

8 the mixing state of LAPs (He et al., 2017, 2018; Painter et al., 2013a; Pu et al., 2017).

9 Therefore, the conversion from satellite spectra to ground concentrations of LAPs will

10 cause significant errors.

11 3.2.4. Retrieval of Radiative Forcing by LAPs in Snow

12 Instantaneous surface solar irradiance at the time of MODIS overpass in January-

13 February is simulated using the SBDART model (Ricchiazzi et al., 1998) with MODIS

14 AOD data as inputs. Wang et al. (2017) has validated the MODIS AOD data using in

15 situ measurements in NEC. For the other inputs, the typical values for mid-latitude

16 winter provided by SBDART are used. As a result, the normalized mean bias (NMB)

17 is less than 2% (Figure S1).

18 We estimate the instantaneous spectrally-integrated radiative forcing at the surface by

19 LAPs in snow (RF_{MODIS}^{LAPs}) under clear-sky conditions at the time of MODIS Aqua

20 overpass, which is a function of solar irradiance and the difference between the MODIS

21 spectral reflectance and a simulated clean-snow ($R_{\lambda}^{clean-snow}$) reflectance (Miller et al.,

22 2016). $R_{\lambda}^{clean-snow}$ is simulated using SNICAR model based on the retrieved R_{eff} and

1 MODIS derived solar zenith angle (θ). On the other hand, for MODIS spectral

2 reflectance, because MODIS provides only discrete reflectances, we simulate a

3 continuous spectral reflectance by fitting SNICAR to the MODIS data and derive the

4 fitting parameters by minimizing the RMSE (Painter et al., 2009):

$$\text{RMSE} = \left(\frac{1}{4} \sum_{\lambda=\text{band1}}^{\text{band4}} (R_\lambda^{\text{model}} - R_\lambda^{\text{MODIS}})^2 \right)^{1/2} \qquad (3)$$

6 where RMSE is the root mean squared error; and R_λ^{model} and R_λ^{MODIS} represent the

7 simulated and MODIS-derived reflectances at a wavelength λ. Thus, $\text{RF}_{\text{MODIS}}^{\text{LAPs}}$ is

8 expressed as follows:

$$\text{RF}_{\text{MODIS}}^{\text{LAPs}} = \sum_{\lambda=300\,\text{nm}}^{1240\,\text{nm}} E_\lambda * D_\lambda * \Delta\lambda \qquad (4)$$

10 where E_λ is the solar irradiance at a wavelength λ simulated by SBDART model; D_λ

11 is the difference between the clean-snow ($R_\lambda^{\text{clean-snow}}$) and simulated reflectances (R_λ^{model})

12 at a wavelength λ; and $\Delta\lambda$ is 10 nm.

13 3.2.5. Uncertainties

14 The uncertainties in radiative forcing retrievals are primarily due to terrain, liquid snow

15 water, snow patchiness, protrusion of vegetation and atmospheric correction. The study

16 areas are located on smooth plains, and the content of liquid snow water is limited in

17 the study regions in January and February (Wang et al., 2013). Moreover, both

18 experimental and theoretical evidences show that the effect of liquid water in snow on

19 snow reflectance is small in the shortwave part of the spectrum but obvious at the

20 wavelengths of 0.95 μm and 1.15 μm (O'Brien and Munis, 1975; O'Brien and Koh,

21 1981; Wiscombe and Warren 1980), which are not included in MODIS bands used in

1 our study. As a result, the effect of liquid water in snow on the calculations of snow

2 grain size, I_{LAPs} and radiative forcing are limited. Therefore, the effects of terrain and

3 liquid snow water on MODIS retrievals could be negligible.

4 In our study, the snow-covered area is determined if the NDSI and the reflectance in

5 band 4 both exceed 0.6, which means that fractional snow cover (FSC) is larger than

6 0.87 according to the FSC equation (FSC= -0.01 + 1.45 *NDSI) from the MODIS Snow

7 Products Collection 6 User Guide (http://nsidc.org/data/MYD10A1). In January and

8 February, snow depth is much high and reaches its maximum depth in NEC, snow

9 patchiness in high snow-covered areas is mostly due to the protrusion of vegetation

10 according to the observations of field campaigns (Wang et al., 2013, 2014a). So that

11 the MODIS derived surface reflectance (R_λ^{MODIS}) in a pixel of our study areas is not

12 snow reflectance, but a mixture of snow and vegetation reflectance. Therefore, we need

13 to correct the errors of snow reflectance caused by the protrusion of vegetation.

14 According to Painter et al. (2009), R_λ^{MODIS} could be expressed as:

$$R_\lambda^{MODIS} = \frac{E_\lambda * FSC * R_{snow}^\lambda + E_\lambda * (1\text{-}FSC) * R_{vegetation}^\lambda}{E_\lambda}$$

$$= FSC * R_{snow}^\lambda + (1\text{-}FSC) * R_{vegetation}^\lambda \qquad (5)$$

17 where R_λ^{MODIS} is MODIS derived surface reflectance at a wavelength λ, E_λ is solar

18 irradiance at a wavelength λ. FSC is the fractional snow cover, which could be derived

19 according to the FSC equation. R_{snow}^λ and $R_{vegetation}^\lambda$ represent snow and vegetation

20 reflectance, respectively, at a wavelength λ. $R_{vegetation}^\lambda$ is from the study of Siegmund

21 and Menz (2005). Then R_{snow}^λ could be expressed as:

1 $$R^{\lambda}_{snow} = \frac{(R^{MODIS}_{\lambda}-(1-FSC)*R^{\lambda}_{vegetation})}{FSC} \qquad (6)$$

2 Finally, the accuracy of MODIS surface reflectance (MYD09GA) due to atmospheric

3 correction is typically calculated based on the MODIS Surface Reflectance User's

4 Guide (Collection 6, https://modis.gsfc.nasa.gov/data/dataprod/mod09.php) as follows:

5 $$\pm \ (0.005 + 0.05*reflectance)$$

6 which is suitable under conditions that AOD is less than 5.0 and θ is less than 75°.

7 Therefore, we also estimate the uncertainty of MODIS retrievals from atmospheric

8 correction. Briefly, the MODIS derived snow reflectance ($R^{\lambda}_{snow, \ uncertainty}$), which takes

9 into an account of the accuracy of the atmospheric correction, is expressed as:

10 $$R^{\lambda}_{snow, \ uncertainty} = R^{\lambda}_{snow}\pm (0.005 + 0.05*R^{\lambda}_{snow}) \qquad (7)$$

11 then, the fractional uncertainty of MODIS retrieved snow grain size ($FU_{R_{eff}}$) could be

12 expressed as:

14 $$FU_{R_{eff}}=\frac{R_{eff, \ uncertainty}-R_{eff}}{R_{eff}} \qquad (8)$$

16 where $R_{eff, \ uncertainty}$ is the SNICAR simulated snow grain size using the snow

17 reflectance of $R^{1240}_{snow, \ uncertainty}$. Similar to snow grain size, the fractional uncertainty of

18 I_{LAPs} ($FU_{I_{LAPs}}$) and RF^{LAPs}_{MODIS} (FU_{RF}) is:

19 $$FU_{I_{LAPs}}=\frac{I_{LAPs, \ uncertainty}-I_{LAPs}}{I_{LAPs}} \qquad (9)$$

20 $$FU_{RF}=\frac{RF^{LAPs}_{MODIS, \ uncertainty} -RF^{LAPs}_{MODIS}}{RF^{LAPs}_{MODIS}} \qquad (10)$$

21 We note that the positive and negative uncertainty is asymmetric due to the nonlinearity

22 of SNICAR model.

23 3.2.6. Attribution of the Spatial Variance of Radiative Forcing by LAPs in Snow

1   As discussed above, RF_{MODIS}^{LAPs} is dependent on I_{LAPs}, R_{eff} and θ, and could be

2   expressed as:

3                  $RF_{MODIS}^{LAPs}=f\left(I_{LAPs}, R_{eff}, \theta\right)$ (11)

4   as a result, the spatial patterns of I_{LAPs}, R_{eff} and θ determine the spatial pattern of

5   RF_{MODIS}^{LAPs}. Firstly, we keep R_{eff} and θ spatially constant with values of the spatial

6   averages ($\overline{R_{eff}}$ and $\overline{\theta}$). Therefore, the spatial pattern of radiative forcing is only

7   dependent on the distribution of I_{LAPs}:

8                  $RF_{MODIS}^{LAPs}(I_{LAPs})=f\left(I_{LAPs}, \overline{R_{eff}}, \overline{\theta}\right)$ (12)

9   similarly, we could obtain another two equations:

10                $RF_{MODIS}^{LAPs}(R_{eff})=f\left(\overline{I_{LAPs}}, R_{eff}, \overline{\theta}\right)$ (13)

11                $RF_{MODIS}^{LAPs}(\theta)=f\left(\overline{I_{LAPs}}, \overline{R_{eff}}, \theta\right)$ (14)

12   Then RF_{MODIS}^{LAPs} is regressed with $RF_{MODIS}^{LAPs}(I_{LAPs})$, $RF_{MODIS}^{LAPs}(R_{eff})$ and $RF_{MODIS}^{LAPs}(\theta)$ using

13   multiple linear regression, the regressed radiative forcing ($RF_{Regression}^{LAPs}$) is expressed as:

14        $RF_{Regression}^{LAPs}=a+b*RF_{MODIS}^{LAPs}(I_{LAPs})+c*RF_{MODIS}^{LAPs}(R_{eff})+d*RF_{MODIS}^{LAPs}(\theta)$ (15)

15   where a, b, c and d are regression coefficients. In our study, we find that $RF_{Regression}^{LAPs}$

16   could explained 99.9% of the variance of RF_{MODIS}^{LAPs} (Figure S2). Therefore, we can

17   attribute the variance of $RF_{Regression}^{LAPs}$ instead of RF_{MODIS}^{LAPs} to estimate the fractional

18   contribution of I_{LAPs}, R_{eff} and θ to radiative forcing. Equation 15 can be written as:

19    $RF_{Regression}^{LAPs}- \overline{RF_{Regression}^{LAPs}}=b*(RF_{MODIS}^{LAPs}(I_{LAPs})-\overline{RF_{MODIS}^{LAPs}(I_{LAPs})})+c*(RF_{MODIS}^{LAPs}(R_{eff})-$

20            $\overline{RF_{MODIS}^{LAPs}(R_{eff})})+d*(RF_{MODIS}^{LAPs}(\theta)-\overline{RF_{MODIS}^{LAPs}(\theta)})$ (16)

21   where, $RF_{Regression}^{LAPs}- \overline{RF_{Regression}^{LAPs}}$ is radiative forcing anomaly ($RF_{Regression, anomaly}^{LAPs}$). Then,

22   Equation 16 can be written as:

1    $RF_{\text{Regression, anomaly}}^{\text{LAPs}} = b*RF_{\text{MODIS, anomaly}}^{\text{LAPs}}(I_{\text{LAPs}}) + c*RF_{\text{MODIS, anomaly}}^{\text{LAPs}}(R_{\text{eff}}) +$

2    $\qquad\qquad d*RF_{\text{MODIS, anomaly}}^{\text{LAPs}}(\theta)$ $\qquad\qquad\qquad\qquad\qquad$ (17)

3   according to Huang et al. (2016) and Huang and Yi (1991), the fractional contribution

4   of I_{LAPs} to the variance of radiative forcing ($FC_{I_{\text{LAPs}}}$) can be expressed as:

5    $FC_{I_{\text{LAPs}}} =$

6    $\dfrac{1}{m}\displaystyle\sum_{i=1}^{m}\left(\dfrac{(b*RF_{\text{MODIS, anomaly}}^{\text{LAPs}}(I_{\text{LAPs}})_i)^2}{(b*RF_{\text{MODIS, anomaly}}^{\text{LAPs}}(I_{\text{LAPs}})_i)^2 + (c*RF_{\text{MODIS, anomaly}}^{\text{LAPs}}(R_{\text{eff}})_i)^2 + (d*RF_{\text{MODIS, anomaly}}^{\text{LAPs}}(\theta)_i)^2}\right)$

7    $\qquad\qquad\qquad\qquad\qquad\qquad\qquad\qquad\qquad\qquad\qquad\qquad\qquad$ (18)

8   where, m is the length of the data series. Similarly, we can obtain $FC_{R_{\text{eff}}}$ and FC_{θ}.

9   3.2.7. Calculation of In situ Radiative Forcing by LAPs in Snow

10   $RF_{\text{MODIS}}^{\text{LAPs}}$ should be validated with measurements. However, due to the lack of radiative

11   forcing measurements in NEC, we estimate the in situ radiative forcing ($RF_{\text{in situ}}^{\text{estimated}}$) from

12   measured BC_{equiv} values. Briefly, we use SNICAR to calculate the in situ reduction in

13   snow albedo from BC_{equiv} and MODIS retrieved R_{eff}. Then, the SBDART model is

14   used to estimate $RF_{\text{in situ}}^{\text{estimated}}$.

15   4. Results

16   4.1. The spatial distribution of AOD and BC emission

17   Northeastern China suffers from heavy local pollutant emissions with high aerosol mass

18   concentrations in winter (Wiedensohler et al., 2009). Figure 2a shows the spatial

19   distribution of AOD at 550 nm derived from MODIS in NEC. We can find that AOD

20   in the studying areas range from 0.08 to 0.65 and show strong spatial inhomogeneity.

21   The largest AOD values are found in industrial areas at the south central of NEC, where

1   are the largest urban areas of NEC with the major cities of Harbin, Changchun, and

2   Shenyang. These areas are associated with the largest pollution emission and

3   anthropogenic activities in NEC (Wang et al., 2017). By comparison, the MODIS-Aqua

4   results show that the AOD in the west of NEC along the border of China is smallest.

5   Similar patterns of AOD were also found by Zhang et al. (2013) and Zhao et al. (2014).

6   Previous studies indicated that BC are the primary light-absorbing particles in

7   atmosphere (Cao et al., 2006) and seasonal snow (Wang et al., 2013). Figure 2b shows

8   the spatial distribution of BC emission density in January-February of 2010 in NEC.

9   The pattern of BC emission density is very comparable to AOD with the highest values

10   of $> 5*10^4$ g km^{-2} month^{-1} in south central NEC and the lowest values of $< 5*10^2$ g km^{-}

11   ^{2} month^{-1} in the remote areas of northwestern China. Both the results of AOD and BC

12   emission density imply that the seasonal snow in south central of NEC suffers from

13   abundant BC deposition and the radiative forcing by LAPs in snow is likely to be

14   highest in NEC.

15   4.2. The spatial distribution of snowfall frequency and land cover types

16   Snowfall is spatially varied in NEC and has a dominated effect on local fractional snow

17   cover, then defined snow-covered areas, where we retrieved the radiative forcing by

18   LAPs in snow in our study. Figure 3a shows the normalized snowfall frequency in

19   January-February from 2003 to 2017. We can find that the highest snowfall frequency

20   occurred in northwestern and southeastern NEC, where are forest-covered areas (see

21   Figure 3b). In contrast, the areas from central to southwestern NEC present lowest

22   snowfall frequency, which means that the fractional snow cover in these areas is likely

1 to be lower than other areas and unable to reach to the critical value that we used to

2 define the snow-covered areas. On the other hand, land cover types will also affect the

3 local fractional snow cover. From Figure 3b, we can find that NEC presents a spatially

4 different land cover types, the main land cover types are grasslands, croplands and

5 evergreen needle leaf (forests). Grasslands and croplands are mainly located in

6 southwestern NEC and central NEC respectively, while forests are distributed in

7 northern and southeastern NEC. In our study periods, grasslands and croplands have

8 limited influence on snow cover. However, in forest areas, even completed covered by

9 deep snow, forest will effectively affect the derived surface reflectance from MODIS-

10 Aqua satellite, then the determination of snow-covered areas (further discussions in

11 Section 5).

12 4.3. Radiative Forcing by LAPs in Snow

13 Figure 4 shows the identified snow-covered areas, which are primarily concentrated

14 between 40 °N and 50 °N. Consistent with our analysis above, the low snow-frequency

15 areas of south central and southwestern NEC and forest-covered areas of northern and

16 southeastern NEC are not identified as snow-covered areas. According to the

17 geographical distribution (Figure 4a), we separated the studied areas into three regions:

18 western NEC (WNEC), central NEC (CNEC) and eastern NEC (ENEC).

19 The spatial distributions of I_{LAPs}, R_{eff}, and RF_{MODIS}^{LAPs} are displayed in Figure 4, and

20 their statistics are presented in Figure 5. On average, I_{LAPs} is ~0.27±0.045; R_{eff} is

21 ~261±32 μm; and RF_{MODIS}^{LAPs} is ~45.1±6.8 W m^{-2} in NEC. Regionally, RF_{MODIS}^{LAPs} is

22 largest and shows an average of ~50.9±4.2 W m^{-2} in CNEC, where is located in the

1 industrial areas and closed to the largest urban areas of NEC, therefore suffers from the

2 most serious pollutant emissions among these three regions. ENEC displays the second

3 largest radiative forcing with an average RF^{LAPs}_{MODIS} of ~45.7±4.5 W m^{-2}. The lowest

4 value of ~41.0±5.9 W m^{-2} occurs in WNEC, where both AOD and BC emission density

5 are lowest compared with other two regions, which is not only due to the low local

6 pollutant emissions but also because that the regional transport of this region in our

7 study period is mostly from the clean northwest and suffer from little influence of

8 human activities (Wang et al., 2014b). For the individual regions, RF^{LAPs}_{MODIS} presents an

9 increase from north to south in CNEC that ranges from 40.4 to 64.6 W m^{-2}. In ENEC

10 an east-west gradient of RF^{LAPs}_{MODIS} is noted that ranges from 62.0 to 35.0 W m^{-2}. The

11 most distinct intra-regional difference is in WNEC, where RF^{LAPs}_{MODIS} ranges from 22.3

12 W m^{-2} to 55.5 W m^{-2}. Generally, the patterns are consistent with those of AOD and BC

13 emission density in NEC. Moreover, the spatial pattern of radiative forcing by LAPs in

14 snow in this study is comparable with the results by Zhao et al. (2014), who firstly

15 estimated the radiative forcing of LAPs in snow through WRF model and found that

16 the radiative forcing in industrial source regions such as southern CNEC is obviously

17 much higher than that in border regions such as WNEC, which primarily resulted from

18 the spatial differences of LAP dry and wet deposition. Compared with the results from

19 other studies, Seidel et al. (2016) reported a radiative forcing of ~20 W m^{-2} in the Sierra

20 Nevada in late February, which is lower than the result in NEC, eventhough the surface

21 solar irradiance in Sierra Nevada is higher. Painter et al. (2013b) reported an average

22 radiative forcing of 215±63 W m^{-2} in the Senator Beck Basin Study Area (SBBSA),

1 SW Colorado, USA, which is approximately four times of our retrieved radiative

2 forcing near industrial areas in NEC. However, the snow grain size and the surface solar

3 irradiance in their study period is larger than that in our study by a factor of >2.5 and >4,

4 respectively. The results implied the abundant LAP content in snow of CNEC. The

5 regional and intra-regional patterns of variability in I_{LAPs} are quite similar to those of

6 RF_{MODIS}^{LAPs}, which indicates the significant role of LAP content in determining the spatial

7 distribution of radiative forcing; the average values of I_{LAPs} are ~0.311±0.024 in

8 CNEC, ~0.307±0.026 in ENEC, and ~0.238±0.031 in WNEC. In contrast to I_{LAPs} and

9 RF_{MODIS}^{LAPs}, R_{eff} displays a smaller spatial variance and presents average values of ~285

10 ±16 μm, ~281±15 μm, and ~239±29 μm in CNEC, ENCE and WNEC, respectively.

11 R_{eff} in WNEC is a little smaller compared with those in other two regions, which is

12 probably due to the higher snowfall frequency, because higher snowfall frequency

13 indicates longer duration of fresh finer snow at surface (Wang et al., 2013; Seidel et al.,

14 2016).

15 Figure 6 shows the average uncertainties of I_{LAPs}, R_{eff} and RF_{MODIS}^{LAPs} due to

16 atmospheric correction in NEC in January-February from 2003 to 2017. The positive

17 (negative) uncertainties of retrieved I_{LAPs} and RF_{MODIS}^{LAPs} from atmospheric correction

18 are comparable and range from 9% to 43% (-10% to -47%) and 14% to 57% (-14% to

19 -47%), respectively. Both of I_{LAPs} and RF_{MODIS}^{LAPs} show larger uncertainties as their

20 values are smaller; the positive (negative) uncertainties of I_{LAPs} and RF_{MODIS}^{LAPs} are

21 largest in WNEC and show averages of 21% (-24%) and 30% (-28%), while the lowest

22 uncertainties of 13% (-15%) and 20% (-20%) for I_{LAPs} and RF_{MODIS}^{LAPs} are found in

1   CNEC. It is because that the uncertainty of snow albedo from atmospheric correction

2   is almost similar in our study areas across the whole NEC region as discussed in Section

3   3.6, however the snow albedo reduction is smaller in clean snow and larger in polluted

4   snow, which results into a larger relative uncertainty of snow albedo reduction in clean

5   snow and a smaller relative uncertainty in polluted snow according to Equation 8. The

6   positive (negative) uncertainties of R_{eff} are smaller compared with I_{LAPs} and

7   RF_{MODIS}^{LAPs}, and range from 14 to 18% (-12% to -16%), which is comparable with the errors

8   between MODIS retrieved and in situ measured snow grain size discussed in Section

9   3.2.2. Moreover, the uncertainties are spatially quite consistent for R_{eff}, which is

10 different from I_{LAPs} and RF_{MODIS}^{LAPs}. We note that the positive and negative uncertainties

11 of all I_{LAPs}, R_{eff}, and RF_{MODIS}^{LAPs} are asymmetric, which are primarily due to the

12 nonlinear characteristics of the radiative transfer in SNICAR model (Painter et al.,

13 2007).

14 As discussed in Section 3, the spatial distribution of RF_{MODIS}^{LAPs} depends on I_{LAPs}, R_{eff}

15 and θ. Even though some studies have successfully retrieved the radiative forcing by

16 LAPs in snow using remote sensing (e.g. Painter et al., 2012a, 2013b). However, none

17 of them has quantitatively estimate what degree of certainty can the variations of

18 radiative forcing be attributed to LAPs in snow. Then we would like to qualify the

19 contribution of each factor to the spatial variance of RF_{MODIS}^{LAPs}. Combing sensitive test

20 and the method of Huang and Yi (1991) as discussed in 3.2.6, we estimate the fractional

21 contribution of I_{LAPs}, R_{eff} and θ to the spatial variance of RF_{MODIS}^{LAPs} in our study areas

22 across NEC (Figure 7). We can find that the contributions from LAPs is largest with a

1   value of 74.6%, while R_{eff} and θ make contributions of 21.2% and 4.2%, respectively

2   in NEC. The result indicates that the LAP content in snow plays a dominant role in

3   determining the spatial distribution of RF_{MODIS}^{LAPs}. Regionally, the contribution of LAPs

4   in WNEC (62.1%) is smaller than those of 73.9% and 83.4% in CNEC and ENEC,

5   while R_{eff} shows a higher contribution of 28.1% in WNEC than those of 19.6% and

6   13.9% in CNEC and ENEC. The results point out a less important effect of LAPs but

7   more important effect of R_{eff} on the spatial distribution of RF_{MODIS}^{LAPs} in WNEC

8   compared with those in CNEC and ENEC. In addition, the contribution of θ is smaller

9   in ENCE (2.7%) than those of 9.8% and 6.5% in WNEC and CNEC, which is primary

10 due to the smallest altitude range of ENEC among those three regions.

11 Seidel et al. (2016) reported that the variations in LAP contents in snow are dominated

12 by LAP deposition and snowfall. Previous studies have also reported that BC is the

13 dominant LAP type in NEC (Wang et al., 2013). Zhao et al. (2014) simulated LAP

14 content and their radiative forcing in seasonal snow using WRF-Chem coupled with

15 SNICAR model and indicated that the radiative forcing by LAPs in snow in NEC is

16 primarily due to BC. Therefore, to examine the spatial distributions of retrieved I_{LAPs}

17 and RF_{MODIS}^{LAPs}, we display the distribution of snowfall (Figure 3a) and BC dry and wet

18 deposition (Figure 8). BC dry deposition is highest in the largest urban areas of NEC

19 with the major cities of Harbin, Changchun, and Shenyang, then decrease sharply

20 outwards from the central of urban areas to remote areas (Figure 8a). Different from

21 BC dry deposition, which is dominated by BC concentrations in the atmosphere, BC

22 wet deposition is affected by both BC concentrations and precipitation and shows an

increase from northwest to southeastern. Generally, the spatial patterns of BC dry and

wet deposition are similar with I_{LAPs} and RF_{MODIS}^{LAPs}. For example, areas with higher BC

dry and wet deposition such as industrial polluted NEC show higher I_{LAPs} and

RF_{MODIS}^{LAPs}. Moreover, from Figure 9a-c, we can find that the correlations between I_{LAPs}

with BC dry and wet deposition and snowfall (R^2=0.65, 0.71, and 0.19) are significant

at the 99% confidence level. The correlations of I_{LAPs} with BC dry and wet deposition

in WNEC is relatively lower than those in CNCE and ENEC, which is partly due to the

effect of dust in this region (Wang et al., 2013; Zhao et al, 2014). Furthermore, using

the method of multiple linear regression, we fitted I_{LAPs} using BC dry and wet

deposition and snowfall data. Figure 9d shows the scatterplots of I_{LAPs} and fitted I_{LAPs}.

We can find that BC dry and wet deposition and snowfall could totally explain 81% of

the spatial variance of I_{LAPs}. The result confirms the reasonability of the spatial patterns

of retrieved I_{LAPs} and thus RF_{MODIS}^{LAPs} in NEC.

4.4. Comparisons of MODIS-Retrieved and In situ Estimated Radiative Forcing by

LAPs in Snow

Figure 10 shows the distribution of the sample sites and the measured BC_{equiv}

concentration in surface snow at each site. Circles and squares represent the snow

samples collected in 2010 (Wang et al., 2013) and 2014 (Wang et al., 2017),

respectively. Generally, BC_{equiv} concentration ranges mostly from ~0.1 to ~3.0 μg g^{-1}

and shows an increase from northwest to southeastern. The highest BC_{equiv}

concentration are found in CNEC while lowest in WNEC. Figure 11a displays a

comparison of MODIS retrieved radiative forcing (RF_{MODIS}^{LAPs}) and in situ radiative forcing

1 ($RF_{in\ situ}^{estimated}$) estimated based on measured BC_{equiv} concentration. In general, the mean

2 absolute error (MAE) for RF_{MODIS}^{LAPs} against $RF_{in\ situ}^{estimated}$ is 15.3 W m^{-2}. The ratios of

3 RF_{MODIS}^{LAPs} to $RF_{in\ situ}^{estimated}$ ($R_{in\ situ}^{MODIS}$) fall mainly in the range of 1-2. The errors indicate larger

4 positive at lower $RF_{in\ situ}^{estimated}$ values, whereas smaller biases are noted at higher $RF_{in\ situ}^{estimated}$

5 values. The results of this bias analysis are comparable with those reported by Painter

6 et al. (2012a). Figure 11b shows a scatterplot of $R_{in\ situ}^{MODIS}$ versus BC_{equiv}. We can find

7 that $R_{in\ situ}^{MODIS}$ and BC_{equiv} display a good correlation; the best-fitting equation is

8 $R_{in\ situ}^{MODIS}=1.690*BC_{equiv}^{-0.522}$, and the R^2 is 0.89 (99% confidence level). This result

9 indicates that the biases in the RF_{MODIS}^{LAPs} retrievals are negatively correlated with the

10 LAP concentrations in NEC. Considering that the typical concentration of BC_{equiv} in

11 clean snow in NEC is 0.15 µg g^{-1}, the bias in RF_{MODIS}^{LAPs} can be as high as 350% in some

12 areas, such as WNEC. In other areas with very polluted snow, such as southern CNEC

13 (where the BC_{equiv} values are typically 2.5 µg g^{-1}), the bias is ~5%. Thus, considering

14 the values reported by Wang et al. (2013, 2017), the biases in RF_{MODIS}^{LAPs} largely fall in

15 the range of ~5% to ~350% in NEC. Comparing Figure 11 with Figure 6, we find that

16 the biases in the RF_{MODIS}^{LAPs} in polluted snow are comparable with the uncertainties of

17 RF_{MODIS}^{LAPs} due to atmospheric corrections. However, in clean snow, the uncertainties

18 from atmospheric corrections could not sufficiently explain the biases in retrieved

19 RF_{MODIS}^{LAPs}. There are three probable reasons: (a) for clean snow, retrieved radiative

20 forcing is very sensitive to MODIS derived surface snow reflectance (Equation 4),

21 although we have corrected the errors of snow reflectance from the protrusion of

22 vegetation in our study areas of high snow cover fractions, the uncertainties from

1   fractional snow cover (FSC) calculation and the vegetation reflectance will effectively

2   influence the corrections of snow reflectance (Equation 5); (b) Painter et al. (2012b)

3   validated the retrieved radiative forcing by LAPs in snow in the Upper Colorado River

4   Basin using in situ estimates based on radiation towers, and also found that the biases

5   in the case of low radiative forcing could be up to several folds. They pointed out that

6   MODIS can not proceed a continuous spectral measurement of a continuously variable

7   forcing like that which LAPs afford to snow albedo due to the variably spaced and

8   discrete bands of MODIS, which prevents a more quantitative retrieval and thus results

9   into a non-negligible uncertainty in radiative forcing retrieval; (c) We use the average

10 of MODIS retrieved radiative forcing in a pixel size of $0.05° \times 0.05°$ to compare with

11 the in situ radiative forcing calculated using observed BC_{equiv} concentration with the

12 sample site located in the center of the pixel. Such a comparison may not be true in

13 some sites due to the inhomogeneous spatial distribution of snow and LAP contents,

14 which will influence radiative forcing estimates, especially in clean snow (Zhao et al.

15 2014). Therefore, we note that the number of sample sites is still limited and more field

16 campaigns are needed to validate the accuracy of MODIS retrievals and then correct

17 the retrieved radiative forcing.

18 4.5. Limitations

19 The determination of snow-covered areas represents a limitation of the method used in

20 this study, which restricts our study to areas with high snow cover fractions; thus, we

21 cannot estimate RF_{MODIS}^{LAPs} across the NEC as a whole. In the future, we will attempt to

22 use the spectral differences between different land cover types to distinguish the

1   spectral reflectance of snow in mixed pixels. This improvement will permit us to

2   expand our work to areas with limited snow cover. Another limitation is that we retrieve

3   only the instantaneous radiative forcing at the surface under clear-sky conditions at the

4   time of MODIS overpass, and these measurements do not represent a time-integrated

5   average over the studied period. However, the estimation of temporally resolved

6   radiative forcing is much more difficult, given the significant effects of clouds,

7   atmospheric components, θ, and the time-varying snow reflectance.

8   5. Discussions

9   In our study, we didn't retrieve the radiative forcing in the northern and southeastern

10 parts of NEC. In those regions, snowfall is frequent, the percent of snow cover is very

11 high and snow is also very deep. For example, in the northern NEC, the averaged snow

12 depth is ~ 20 cm, and in the areas near Changbai Mountain of the southeastern NEC,

13 snow depth could be up to ~ 40 cm (Wang et al., 2013). However, due to the presence

14 of forest cover, the reflected radiation received by sensor aboard the satellite in those

15 areas is mostly due to trees. For example, Figure 12 shows the true color map of MODIS

16 in NEC at 23 January 2010, we can see that in the northern and southeastern parts of

17 NEC, the observed objects from MODIS are almost trees, not the snowpack under trees,

18 although snow is almost completed covered (Wang et al., 2013). Therefore, in those

19 forest areas, discussing the radiative forcing by LAPs in snow is extremely difficult due

20 to the influence of trees. Bond et al. (2006) also indicated that LAPs in snow masked

21 by forests contributes little to radiative forcing. They further pointed out that model

22 representation of and forcing sensitivity to cover ranges of forests have not been

1   verified, and this is a boundless uncertainty in modeling radiative forcing by LAPs in

2   snow at present. However, most modeling studies which simulated the radiative forcing

3   by LAPs in snow didn't take trees into considerations and estimated the radiative

4   forcing over the whole boreal forest areas in the Northern Hemisphere. For example,

5   Flanner et al. (2007) applied SNICAR model coupled a general circulation model to

6   estimate the radiative forcing and response from BC in snow covered areas over the

7   whole Northern Hemisphere. Nevertheless, due to the presence of trees in the extensive

8   boreal forest areas, the simulated radiative forcing is unreal as the incident radiation is

9   reflected by trees but not by the snowpack. Zhao et al. (2014) simulated BC and dust

10   and their radiative forcing in seasonal snow in North China. They found that the

11   radiative forcing by BC and dust is very high in the southeastern NEC, where are forest

12   areas. But in fact, in those areas the simulated radiative forcing by LAPs is also unreal.

13   Therefore, we note that estimating the radiative forcing by LAPs in forest areas should

14   consider into the influence of trees.

15   6. Conclusions

16   In this study, we retrieve I_{LAPs}, R_{eff}, and RF_{MODIS}^{LAPs} across NEC in January-February

17   from 2003 to 2017 using MODIS data, together with a snow albedo model (SNICAR)

18   and a radiative transfer model (SBDART). On average, I_{LAP} is ~0.27±0.045, R_{eff} is

19   ~261±32 μm, and RF_{MODIS}^{LAPs} is ~45.1±6.8 W m^{-2} in NEC. The distribution of RF_{MODIS}^{LAPs}

20   presents distinct spatial differences; the lowest value is 22.3 W m^{-2}, which occurs in

21   remote western NEC, and the highest value is 64.6 W m^{-2}, which occurs near the

22   industrial areas in central NEC. Both I_{LAPs} and RF_{MODIS}^{LAPs} show larger uncertainties

1   from atmospheric correction as their values are smaller. We make a first attempt to

2   attribute the variations of radiative forcing based on remote sensing. The results point

3   out that I_{LAPs}, R_{eff} and θ make fractional contributions of 74.6%, 21.2% and 4.2% to

4   the spatial variance of RF_{MODIS}^{LAPs} in our study areas across NEC. The result confirms that

5   the LAP content in snow plays a dominant role in determining the spatial distribution

6   of RF_{MODIS}^{LAPs}. We also analyze the distribution of BC dry and wet deposition and snowfall,

7   find that they could totally explained 81% of the spatial variance of I_{LAPs}, which

8   indicates the reasonability of the spatial patterns of I_{LAPs} and thus RF_{MODIS}^{LAPs} in NEC.

9   Finally, we validate the retrieved RF_{MODIS}^{LAPs} values using in situ estimated radiative

10   forcing ($RF_{in\ situ}^{estimated}$). The mean absolute error (MAE) of RF_{MODIS}^{LAPs} against $RF_{in\ situ}^{estimated}$ is

11   15.3 W m^{-2}. The biases in the RF_{MODIS}^{LAPs} retrievals display a negative correlation with

12   the LAP concentrations in NEC. Considering typical concentrations of BC_{equiv}, which

13   range from ~0.15 μg g^{-1} to ~2.5 μg g^{-1}, the biases in RF_{MODIS}^{LAPs} fall primarily within the

14   range of ~5% to ~350% in NEC.

1 Acknowledgements

2 This research was supported by the Foundation for Innovative Research Groups of the

3 National Natural Science Foundation of China (41521004), the National Natural

4 Science Foundation of China under grant (41775144 and 41522505). The National

5 Center for Atmospheric Research is sponsored by the National Science Foundation

6 (USA). We thank M. Flanner for providing an executable version of the SNICAR model

7 and modifying it to accommodate our analysis. We thank C. Dang for her suggestions

8 and comments to this study. MODIS data can be found at https://modis.gsfc.nasa.gov/.

9 Snowfall data can be found at http://apps.ecmwf.int/datasets/data/interim-full-

10 daily/levtype=sfc/. BC deposition data can be found at http://www.ipcc-

11 data.org/sim/gcm_monthly/AR5/Reference-Archive.html. Surface measurement

12 datasets are from [Wang, X., et al. (2013). Black carbon and other light-absorbing

13 impurities in snow across Northern China. Journal of Geophysical Research:

14 Atmospheres, 118(3), 1471-1492. https://doi.org/10.1029/2012JD018291] and [Wang,

15 X., et al. (2017). Observations and model simulations of snow albedo reduction in

16 seasonal snow due to insoluble light-absorbing particles during 2014 Chinese survey.

17 Atmospheric Chemistry and Physics, 17(3), 2279-2296. https://doi.org/10.5194/acp-

18 17-2279-2017].

1 References

2 Bond, T. C., Streets, D. G., Yarber, K. F., Nelson, S. M., Woo, J. H., and Klimont, Z.: A technology-based global

3   inventory of black and organic carbon emissions from combustion, J Geophys Res-Atmos, 109,

4   https://doi.org/10.1029/2003jd003697, 2004.

5 Bond, T. C., Habib, G., and Bergstrom, R. W.: Limitations in the enhancement of visible light absorption due to

6   mixing state, J Geophys Res-Atmos, 111, https://doi.org/10.1029/2006jd007315, 2006.

7 Bond, T. C., Doherty, S. J., Fahey, D. W., Forster, P. M., Berntsen, T., DeAngelo, B. J., Flanner, M. G., Ghan, S.,

8   Karcher, B., Koch, D., Kinne, S., Kondo, Y., Quinn, P. K., Sarofim, M. C., Schultz, M. G., Schulz, M.,

9   Venkataraman, C., Zhang, H., Zhang, S., Bellouin, N., Guttikunda, S. K., Hopke, P. K., Jacobson, M. Z., Kaiser,

10   J. W., Klimont, Z., Lohmann, U., Schwarz, J. P., Shindell, D., Storelvmo, T., Warren, S. G., and Zender, C. S.:

11   Bounding the role of black carbon in the climate system: A scientific assessment, J Geophys Res-Atmos, 118,

12   5380-5552, https://doi.org/10.1002/jgrd.50171, 2013.

13 Cao, G. L., Zhang, X. Y., and Zheng, F. C.: Inventory of black carbon and organic carbon emissions from China,

14   Atmospheric Environment, 40, 6516-6527, https://doi.org/10.1016/j.atmosenv.2006.05.070, 2006.

15 Cohen, J., and Rind, D.: The Effect of Snow Cover on the Climate, J Climate, 4, 689-706,

16   https://doi.org/10.1175/1520-0442(1991)004<0689:Teosco>2.0.Co;2, 1991.

17 Dang, C., and Hegg, D. A.: Quantifying light absorption by organic carbon in Western North American snow by

18   serial chemical extractions, J Geophys Res-Atmos, 119, https://doi.org/10.1002/2014jd022156, 2014.

19 Dang, C., Warren, S. G., Fu, Q., Doherty, S. J., Sturm, M., and Su, J.: Measurements of light-absorbing particles in

20   snow across the Arctic, North America, and China: Effects on surface albedo, J Geophys Res-Atmos, 122,

21   10149-10168, https://doi.org/10.1002/2017jd027070, 2017.

22 Di Mauro, B., Fava, F., Ferrero, L., Garzonio, R., Baccolo, G., Delmonte, B., and Colombo, R.: Mineral dust impact

23   on snow radiative properties in the European Alps combining ground, UAV, and satellite observations, J

24   Geophys Res-Atmos, 120, 6080-6097, https://doi.org/10.1002/2015jd023287, 2015.

25 Di Mauro, B., Baccolo, G., Garzonio, R., Giardino, C., Massabo, D., Piazzalunga, A., Rossini, M., and Colombo,

26   R.: Impact of impurities and cryoconite on the optical properties of the Morteratsch Glacier (Swiss Alps),

27   Cryosphere, 11, 2393-2409, https://doi.org/10.5194/tc-11-2393-2017, 2017.

28 Doherty, S. J., Warren, S. G., Grenfell, T. C., Clarke, A. D., and Brandt, R. E.: Light-absorbing impurities in Arctic

29   snow, Atmospheric Chemistry and Physics, 10, 11647-11680, https://doi.org/10.5194/acp-10-11647-2010,

30   2010.

31 Doherty, S. J., Dang, C., Hegg, D. A., Zhang, R. D., and Warren, S. G.: Black carbon and other light-absorbing

32   particles in snow of central North America, J Geophys Res-Atmos, 119, 12807-12831,

33   https://doi.org/10.1002/2014jd022350, 2014.

34 Dumont, M., Brun, E., Picard, G., Michou, M., Libois, Q., Petit, J. R., Geyer, M., Morin, S., and Josse, B.:

35   Contribution of light-absorbing impurities in snow to Greenland's darkening since 2009, Nat Geosci, 7, 509-

36   512, https://doi.org/10.1038/Ngeo2180, 2014.

37 Flanner, M. G., Zender, C. S., Randerson, J. T., and Rasch, P. J.: Present-day climate forcing and response from

38   black carbon in snow, J Geophys Res-Atmos, 112, https://doi.org/10.1029/2006jd008003, 2007.

39 Flanner, M. G., Zender, C. S., Hess, P. G., Mahowald, N. M., Painter, T. H., Ramanathan, V., and Rasch, P. J.:

40   Springtime warming and reduced snow cover from carbonaceous particles, Atmospheric Chemistry and Physics,

41   9, 2481-2497, https://doi.org/10.5194/acp-9-2481-2009, 2009.

42 Grenfell, T. C., Doherty, S. J., Clarke, A. D., and Warren, S. G.: Light absorption from particulate impurities in snow

43   and ice determined by spectrophotometric analysis of filters, Appl Optics, 50, 2037-2048,

1   https://doi.org/10.1364/Ao.50.002037, 2011.

2   Hadley, O. L., and Kirchstetter, T. W.: Black-carbon reduction of snow albedo, Nat Clim Change, 2, 437-440,

3   https://doi.org/10.1038/nclimate1433, 2012.

4   Hall, D. K., Riggs, G. A., and Salomonson, V. V.: Development of Methods for Mapping Global Snow Cover Using

5   Moderate Resolution Imaging Spectroradiometer Data, Remote Sens Environ, 54, 127-140,

6   https://doi.org/10.1016/0034-4257(95)00137-P, 1995.

7   Hansen, J., and Nazarenko, L.: Soot climate forcing via snow and ice albedos, P Natl Acad Sci USA, 101, 423-428,

8   https://doi.org/10.1073/pnas.2237157100, 2004.

9   He, C. L., Li, Q. B., Liou, K. N., Takano, Y., Gu, Y., Qi, L., Mao, Y. H., and Leung, L. R.: Black carbon radiative

10   forcing over the Tibetan Plateau, Geophys Res Lett, 41, 7806-7813, https://doi.org/10.1002/2014gl062191,

11   2014.

12   He, C. L., Takano, Y., Liou, K. N., Yang, P., Li, Q. B., and Chen, F.: Impact of Snow Grain Shape and Black Carbon-

13   Snow Internal Mixing on Snow Optical Properties: Parameterizations for Climate Models, J Climate, 30,

14   10019-10036, https://doi.org/10.1175/Jcli-D-17-0300.1, 2017.

15   He, C. L., Liou, K. N., Takano, Y., Yang, P., Qi, L., and Chen, F.: Impact of Grain Shape and Multiple Black Carbon

16   Internal Mixing on Snow Albedo: Parameterization and Radiative Effect Analysis, J Geophys Res-Atmos, 123,

17   1253-1268, https://doi.org/10.1002/2017jd027752, 2018.

18   Huang, J. P., and Yi, Y. H.: Inversion of a nonlinear dynamic-model from the observation, Science China Chemistry,

19   34, 1246-1246, 1991.

20   Huang, J. P., Fu, Q., Zhang, W., Wang, X., Zhang, R. D., Ye, H., and Warren, S. G.: Dust and Black Carbon in

21   Seasonal Snow across Northern China, Bulletin of the American Meteorological Society, 92, 175-+,

22   https://doi.org/10.1175/2010bams3064.1, 2011.

23   Huang, J. P., Xie, Y. K., Guan, X. D., Li, D. D., and Ji, F.: The dynamics of the warming hiatus over the Northern

24   Hemisphere, Climate Dynamics, 48, 429-446, https://doi.org/10.1007/s00382-016-3085-8, 2016.

25   Ichoku, C., Levy, R., Kaufman, Y. J., Remer, L. A., Li, R. R., Martins, V. J., Holben, B. N., Abuhassan, N., Slutsker,

26   I., Eck, T. F., and Pietras, C.: Analysis of the performance characteristics of the five-channel Microtops II Sun

27   photometer for measuring aerosol optical thickness and precipitable water vapor, J Geophys Res-Atmos, 107,

28   https://doi.org/10.1029/2001jd001302, 2002.

29   Jacobson, M. Z.: Control of fossil-fuel particulate black carbon and organic matter, possibly the most effective

30   method of slowing global warming, J Geophys Res-Atmos, 107, https://doi.org/10.1029/2001jd001376, 2002.

31   Jacobson, M. Z.: Climate response of fossil fuel and biofuel soot, accounting for soot's feedback to snow and sea ice

32   albedo and emissivity, J Geophys Res-Atmos, 109, https://doi.org/10.1029/2004jd004945, 2004.

33   Kaspari, S., Painter, T. H., Gysel, M., Skiles, S. M., and Schwikowski, M.: Seasonal and elevational variations of

34   black carbon and dust in snow and ice in the Solu-Khumbu, Nepal and estimated radiative forcings,

35   Atmospheric Chemistry and Physics, 14, 8089-8103, https://doi.org/10.5194/acp-14-8089-2014, 2014.

36   Li, C. L., Bosch, C., Kang, S. C., Andersson, A., Chen, P. F., Zhang, Q. G., Cong, Z. Y., Chen, B., Qin, D. H., and

37   Gustafsson, O.: Sources of black carbon to the Himalayan-Tibetan Plateau glaciers, Nat Commun, 7,

38   https://doi.org/10.1038/ncomms12574, 2016.

39   Liou, K. N., Takano, Y., and Yang, P.: Light absorption and scattering by aggregates: Application to black carbon

40   and snow grains, J Quant Spectrosc Ra, 112, 1581-1594, https://doi.org/10.1016/j.jqsrt.2011.03.007, 2011.

41   Liou, K. N., Takano, Y., He, C., Yang, P., Leung, L. R., Gu, Y., and Lee, W. L.: Stochastic parameterization for

42   light absorption by internally mixed BC/dust in snow grains for application to climate models, J Geophys Res-

43   Atmos, 119, 7616-7632, https://doi.org/10.1002/2014jd021665, 2014.

44   Lyapustin, A., Tedesco, M., Wang, Y. J., Aoki, T., Hori, M., and Kokhanovsky, A.: Retrieval of snow grain size

1   over   Greenland   from   MODIS,   Remote   Sens   Environ,   113,   1976-1987,
2   https://doi.org/10.1016/j.rse.2009.05.008, 2009.
3   McConnell, J. R., Edwards, R., Kok, G. L., Flanner, M. G., Zender, C. S., Saltzman, E. S., Banta, J. R., Pasteris, D.
4   R., Carter, M. M., and Kahl, J. D. W.: 20th-century industrial black carbon emissions altered arctic climate
5   forcing, Science, 317, 1381-1384, https://doi.org/10.1126/science.1144856, 2007.
6   Miller, S. D., Wang, F., Burgess, A. B., Skiles, S. M., Rogers, M., and Painter, T. H.: Satellite-Based Estimation of
7   Temporally Resolved Dust Radiative Forcing in Snow Cover, J Hydrometeorol, 17, 1999-2011,
8   https://doi.org/10.1175/Jhm-D-15-0150.1, 2016.
9   Negi, H. S., and Kokhanovsky, A.: Retrieval of snow grain size and albedo of western Himalayan snow cover using
10   satellite data, Cryosphere, 5, 831-847, https://doi.org/10.5194/tc-5-831-2011, 2011.
11   Nolin, A. W., and Dozier, J.: Estimating Snow Grain-Size Using Aviris Data, Remote Sens Environ, 44, 231-238,
12   https://doi.org/10.1016/0034-4257(93)90018-S, 1993.
13   Nolin, A. W., and Dozier, J.: A hyperspectral method for remotely sensing the grain size of snow, Remote Sens
14   Environ, 74, 207-216, https://doi.org/10.1016/S0034-4257(00)00111-5, 2000.
15   O'Brien, H. W., and Munis, R. H.: Red and Near-Infrared Spectral Reflectance of Snow, 311, 1975.
16   O'Brien, H. W., and Koh, G.: Near-infrared reflectance of snow-covered substrates, 1981.
17   Painter, T. H., Roberts, D. A., Green, R. O., and Dozier, J.: The effect of grain size on spectral mixture analysis of
18   snow-covered area from AVIRIS data, Remote Sens Environ, 65, 320-332, https://doi.org/10.1016/S0034-
19   4257(98)00041-8, 1998.
20   Painter, T. H., Barrett, A. P., Landry, C. C., Neff, J. C., Cassidy, M. P., Lawrence, C. R., McBride, K. E., and Farmer,
21   G. L.: Impact of disturbed desert soils on duration of mountain snow cover, Geophys Res Lett, 34,
22   https://doi.org/10.1029/2007gl030284, 2007.
23   Painter, T. H., Rittger, K., McKenzie, C., Slaughter, P., Davis, R. E., and Dozier, J.: Retrieval of subpixel snow
24   covered   area,   grain   size,   and   albedo   from   MODIS,   Remote   Sens   Environ,   113,   868-879,
25   https://doi.org/10.1016/j.rse.2009.01.001, 2009.
26   Painter, T. H., Deems, J. S., Belnap, J., Hamlet, A. F., Landry, C. C., and Udall, B.: Response of Colorado River
27   runoff   to   dust   radiative   forcing   in   snow,   P   Natl   Acad   Sci   USA,   107,   17125-17130,
28   https://doi.org/10.1073/pnas.0913139107, 2010.
29   Painter, T. H., Bryant, A. C., and Skiles, S. M.: Radiative forcing by light absorbing impurities in snow from MODIS
30   surface reflectance data, Geophys Res Lett, 39, https://doi.org/10.1029/2012gl052457, 2012a.
31   Painter, T. H., Skiles, S. M., Deems, J. S., Bryant, A. C., and Landry, C. C.: Dust radiative forcing in snow of the
32   Upper Colorado River Basin: 1. A 6 year record of energy balance, radiation, and dust concentrations, Water
33   Resour Res, 48, https://doi.org/10.1029/2012wr011985, 2012b.
34   Painter, T. H., Flanner, M. G., Kaser, G., Marzeion, B., VanCuren, R. A., and Abdalati, W.: End of the Little Ice
35   Age in the Alps forced by industrial black carbon, P Natl Acad Sci USA, 110, 15216-15221,
36   https://doi.org/10.1073/pnas.1302570110, 2013a.
37   Painter, T. H., Seidel, F. C., Bryant, A. C., Skiles, S. M., and Rittger, K.: Imaging spectroscopy of albedo and
38   radiative forcing by light-absorbing impurities in mountain snow, J Geophys Res-Atmos, 118, 9511-9523,
39   https://doi.org/10.1002/jgrd.50520, 2013b.
40   Peltoniemi, J. I., Gritsevich, M., Hakala, T., Dagsson-Waldhauserova, P., Arnalds, O., Anttila, K., Hannula, H. R.,
41   Kivekas, N., Lihavainen, H., Meinander, O., Svensson, J., Virkkula, A., and de Leeuw, G.: Soot on Snow
42   experiment: bidirectional reflectance factor measurements of contaminated snow, Cryosphere, 9, 2323-2337,
43   https://doi.org/10.5194/tc-9-2323-2015, 2015.
44   Polashenski, C. M., Dibb, J. E., Flanner, M. G., Chen, J. Y., Courville, Z. R., Lai, A. M., Schauer, J. J., Shafer, M.

1 M., and Bergin, M.: Neither dust nor black carbon causing apparent albedo decline in Greenland's dry snow
2   zone: Implications for MODIS C5 surface reflectance, Geophys Res Lett, 42, 9319-9327,
3   https://doi.org/10.1002/2015gl065912, 2015.
4 Pu, W., Wang, X., Wei, H. L., Zhou, Y., Shi, J. S., Hu, Z. Y., Jin, H. C., and Chen, Q. L.: Properties of black carbon
5   and other insoluble light-absorbing particles in seasonal snow of northwestern China, Cryosphere, 11, 1213-
6   1233, https://doi.org/10.5194/tc-11-1213-2017, 2017.
7 Qian, Y., Gustafson, W. I., Leung, L. R., and Ghan, S. J.: Effects of soot-induced snow albedo change on snowpack
8   and hydrological cycle in western United States based on Weather Research and Forecasting chemistry and
9   regional climate simulations, J Geophys Res-Atmos, 114, https://doi.org/10.1029/2008jd011039, 2009.
10 Ramanathan, V., and Carmichael, G.: Global and regional climate changes due to black carbon, Nat Geosci, 1, 221-
11   227, https://doi.org/10.1038/ngeo156, 2008.
12 Ricchiazzi, P., Yang, S. R., Gautier, C., and Sowle, D.: SBDART: A research and teaching software tool for plane-
13   parallell radiative transfer in the Earth's atmosphere, Bulletin of the American Meteorological Society, 79,
14   2101-2114, https://doi.org/10.1175/1520-0477(1998)079<2101:Sarats>2.0.Co;2, 1998.
15 Rittger, K., Painter, T. H., and Dozier, J.: Assessment of methods for mapping snow cover from MODIS, Adv Water
16   Resour, 51, 367-380, https://doi.org/10.1016/j.advwatres.2012.03.002, 2013.
17 Scambos, T. A., Haran, T. M., Fahnestock, M. A., Painter, T. H., and Bohlander, J.: MODIS-based Mosaic of
18   Antarctica (MOA) data sets: Continent-wide surface morphology and snow grain size, Remote Sens Environ,
19   111, 242-257, https://doi.org/10.1016/j.rse.2006.12.020, 2007.
20 Schwarz, J. P., Doherty, S. J., Li, F., Ruggiero, S. T., Tanner, C. E., Perring, A. E., Gao, R. S., and Fahey, D. W.:
21   Assessing Single Particle Soot Photometer and Integrating Sphere/Integrating Sandwich Spectrophotometer
22   measurement techniques for quantifying black carbon concentration in snow, Atmospheric Measurement
23   Techniques, 5, 2581-2592, https://doi.org/10.5194/amt-5-2581-2012, 2012.
24 Seidel, F. C., Rittger, K., Skiles, S. M., Molotch, N. P., and Painter, T. H.: Case study of spatial and temporal
25   variability of snow cover, grain size, albedo and radiative forcing in the Sierra Nevada and Rocky Mountain
26   snowpack derived from imaging spectroscopy, Cryosphere, 10, 1229-1244, https://doi.org/10.5194/tc-10-1229-
27   2016, 2016.
28 Siegmund, A., and Menz, G.: Fernes nah gebracht–Satelliten-und Luftbildeinsatz zur Analyse von
29   Umweltveränderungen im Geographieunterricht. Geographie und Schule, 154(4), 2-10, 2005.
30 Stamnes, K., Tsay, S. C., Wiscombe, W., and Jayaweera, K.: Numerically Stable Algorithm for Discrete-Ordinate-
31   Method Radiative-Transfer in Multiple-Scattering and Emitting Layered Media, Appl Optics, 27, 2502-2509,
32   https://doi.org/10.1364/Ao.27.002502, 1988.
33 Taylor, K. E., Stouffer, R. J., and Meehl, G. A.: An Overview of Cmip5 and the Experiment Design, Bulletin of the
34   American Meteorological Society, 93, 485-498, https://doi.org/10.1175/Bams-D-11-00094.1, 2012.
35 Toon, O. B., Mckay, C. P., Ackerman, T. P., and Santhanam, K.: Rapid Calculation of Radiative Heating Rates and
36   Photodissociation Rates in Inhomogeneous Multiple-Scattering Atmospheres, J Geophys Res-Atmos, 94,
37   16287-16301, https://doi.org/10.1029/JD094iD13p16287, 1989.
38 Vermote, E.: MOD09A1MODIS/Terra Surface Reflectance 8-Day L3 Global 500m SIN Grid V006. NASA EOSDIS
39   Land Processes DAAC, 2015.
40 Wang, X., Doherty, S. J., and Huang, J. P.: Black carbon and other light-absorbing impurities in snow across
41   Northern China, J Geophys Res-Atmos, 118, 1471-1492, https://doi.org/10.1029/2012jd018291, 2013.
42 Wang, X., Xu, B. Q., and Ming, J.: An Overview of the Studies on Black Carbon and Mineral Dust Deposition in
43   Snow and Ice Cores in East Asia, Journal of Meteorological Research, 28, 354-370,
44   https://doi.org/10.1007/s13351-014-4005-7, 2014a.

1   Wang, X., Pu, W., Zhang, X. Y., Ren, Y., and Huang, J. P.: Water-soluble ions and trace elements in surface snow
2   and their potential source regions across northeastern China, Atmospheric Environment, 114, 57-65,
3   https://doi.org/10.1016/j.atmosenv.2015.05.012, 2015.

4   Wang, X., Pu, W., Ren, Y., Zhang, X. L., Zhang, X. Y., Shi, J. S., Jin, H. C., Dai, M. K., and Chen, Q. L.:
5   Observations and model simulations of snow albedo reduction in seasonal snow due to insoluble light-absorbing
6   particles during 2014 Chinese survey, Atmospheric Chemistry and Physics, 17, 2279-2296,
7   https://doi.org/10.5194/acp-17-2279-2017, 2017.

8   Wang, Z. W., Gallet, J. C., Pedersen, C. A., Zhang, X. S., Strom, J., and Ci, Z. J.: Elemental carbon in snow at
9   Changbai Mountain, northeastern China: concentrations, scavenging ratios, and dry deposition velocities,
10   Atmospheric Chemistry and Physics, 14, 629-640, https://doi.org/10.5194/acp-14-629-2014, 2014b.

11   Warren, S. G., and Wiscombe, W. J.: A Model for the Spectral Albedo of Snow .2. Snow Containing Atmospheric
12   Aerosols, J Atmos Sci, 37, 2734-2745, https://doi.org/10.1175/1520-0469(1980)037<2734:Amftsa>2.0.Co;2,
13   1980.

14   Warren, S. G.: Optical-Properties of Snow, Reviews of Geophysics, 20, 67-89,
15   https://doi.org/10.1029/RG020i001p00067, 1982.

16   Warren, S. G.: Impurities in Snow - Effects on Albedo and Snowmelt Review, Annals of Glaciology, 5, 177-179,
17   https://doi.org/10.3189/1984AoG5-1-177-179, 1984.

18   Wiedensohler, A., Cheng, Y. F., Nowak, A., Wehner, B., Achtert, P., Berghof, M., Birmili, W., Wu, Z. J., Hu, M.,
19   Zhu, T., Takegawa, N., Kita, K., Kondo, Y., Lou, S. R., Hofzumahaus, A., Holland, F., Wahner, A., Gunthe, S.
20   S., Rose, D., Su, H., and Poschl, U.: Rapid aerosol particle growth and increase of cloud condensation nucleus
21   activity by secondary aerosol formation and condensation: A case study for regional air pollution in northeastern
22   China, J Geophys Res-Atmos, 114, https://doi.org/10.1029/2008jd010884, 2009.

23   Wiscombe, W. J., and Warren, S. G.: A Model for the Spectral Albedo of Snow .1. Pure Snow, J Atmos Sci, 37,
24   2712-2733, https://doi.org/10.1175/1520-0469(1980)037<2712:Amftsa>2.0.Co;2, 1980.

25   Wuttke, S., Seckmeyer, G., and Konig-Lang, G.: Measurements of spectral snow albedo at Neumayer, Antarctica,
26   Ann Geophys-Germany, 24, 7-21, https://doi.org/10.5194/angeo-24-7-2006, 2006.

27   Xu, B. Q., Cao, J. J., Hansen, J., Yao, T. D., Joswia, D. R., Wang, N. L., Wu, G. J., Wang, M., Zhao, H. B., Yang,
28   W., Liu, X. Q., and He, J. Q.: Black soot and the survival of Tibetan glaciers, P Natl Acad Sci USA, 106, 22114-
29   22118, https://doi.org/10.1073/pnas.0910444106, 2009.

30   Yasunari, T. J., Bonasoni, P., Laj, P., Fujita, K., Vuillermoz, E., Marinoni, A., Cristofanelli, P., Duchi, R., Tartari,
31   G., and Lau, K. M.: Estimated impact of black carbon deposition during pre-monsoon season from Nepal
32   Climate Observatory - Pyramid data and snow albedo changes over Himalayan glaciers, Atmospheric
33   Chemistry and Physics, 10, 6603-6615, https://doi.org/10.5194/acp-10-6603-2010, 2010.

34   Yasunari, T. J., Koster, R. D., Lau, W. K. M., and Kim, K. M.: Impact of snow darkening via dust, black carbon,
35   and organic carbon on boreal spring climate in the Earth system, J Geophys Res-Atmos, 120, 5485-5503,
36   https://doi.org/10.1002/2014jd022977, 2015.

37   Zhang, R., Hegg, D. A., Huang, J., and Fu, Q.: Source attribution of insoluble light-absorbing particles in seasonal
38   snow across northern China, Atmospheric Chemistry and Physics, 13, 6091-6099, https://doi.org/10.5194/acp-
39   13-6091-2013, 2013.

40   Zhao, C., Hu, Z., Qian, Y., Leung, L. R., Huang, J., Huang, M., Jin, J., Flanner, M. G., Zhang, R., Wang, H., Yan,
41   H., Lu, Z., and Streets, D. G.: Simulating black carbon and dust and their radiative forcing in seasonal snow: a
42   case study over North China with field campaign measurements, Atmospheric Chemistry and Physics, 14,
43   11475-11491, https://doi.org/10.5194/acp-14-11475-2014, 2014.

44   Zhou, Y., Wang, X., Wu, X. Q., Cong, Z. Y., Wu, G. M., and Ji, M. X.: Quantifying Light Absorption of Iron Oxides

1   and Carbonaceous Aerosol in Seasonal Snow across Northern China, Atmosphere-Basel, 8,

2   https://doi.org/10.3390/atmos8040063, 2017.
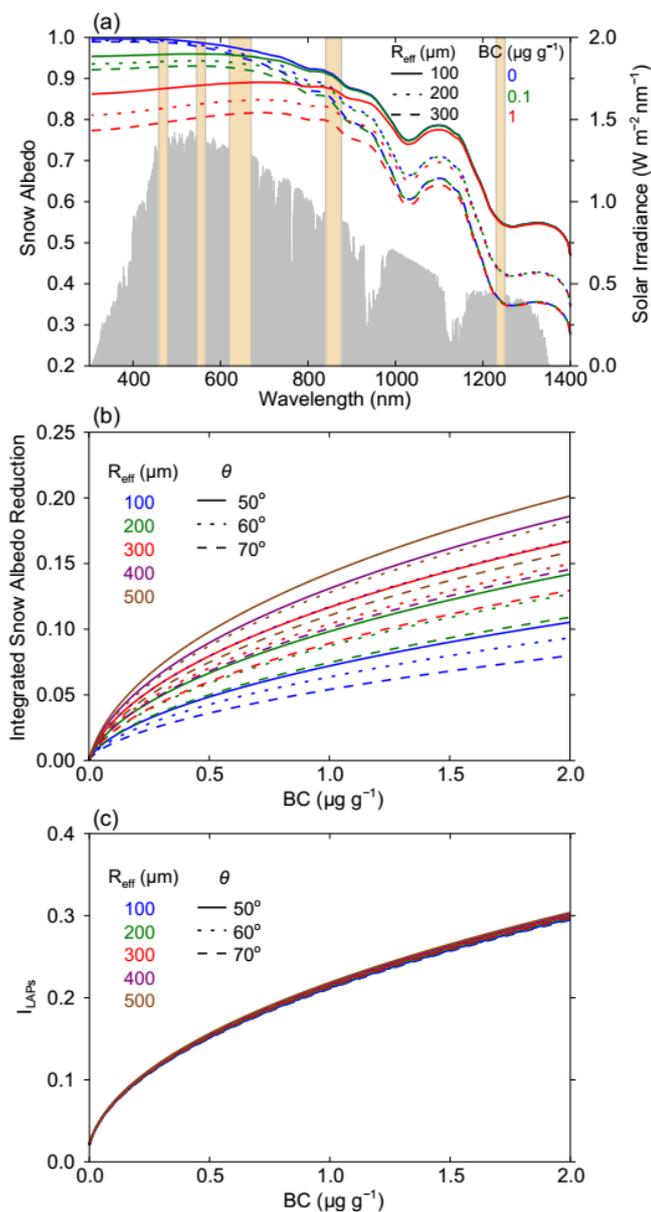
2   **Figure 1**. (a) The spectral albedo of snow with different R_{eff} values and BC contents
3   simulated using SNICAR. The column bars represent MODIS bands, and the gray areas
4   represent the typical solar irradiance in winter in NEC. (b) The reduction in the 300-
5   1240 nm spectral-weighted integrated snow albedo as a function of BC for different
6   R_{eff} values and solar zenith angles (θ) simulated using SNICAR. (c) The variations in
7   the impurity index (I_{LAPs}) with BC content simulated using SNICAR.
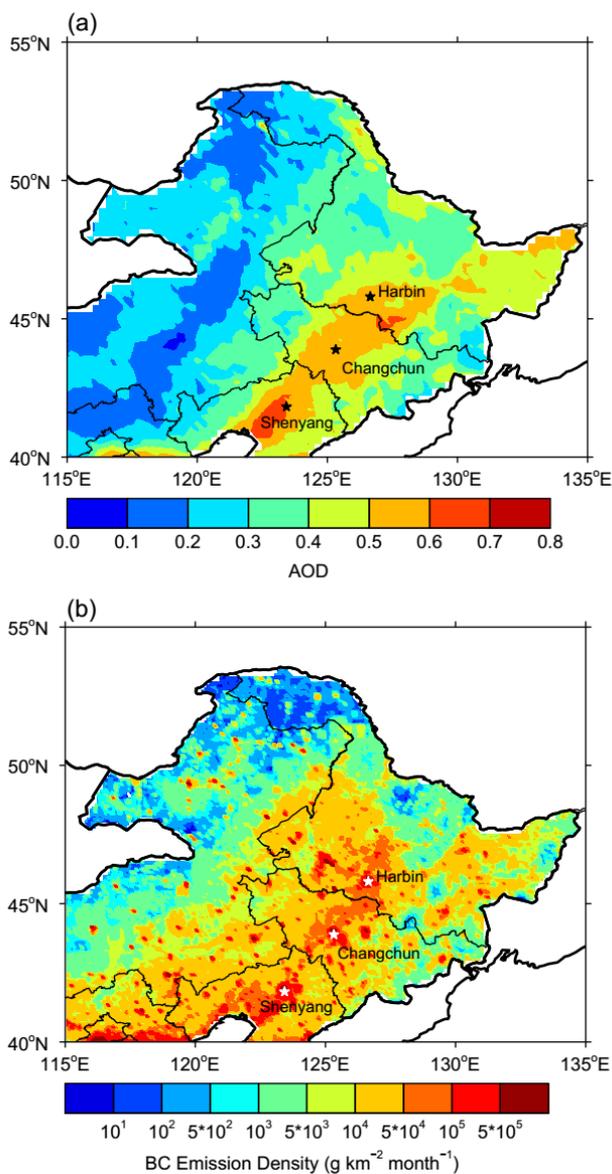
Figure 2. Spatial distribution of (a) MODIS AOD at 550 nm and (b) BC emission
density density in January-February in NEC. AOD data is from 2003 to 2017 and BC
emission density is from 2014. The major cities in NEC are also shown in this figure.
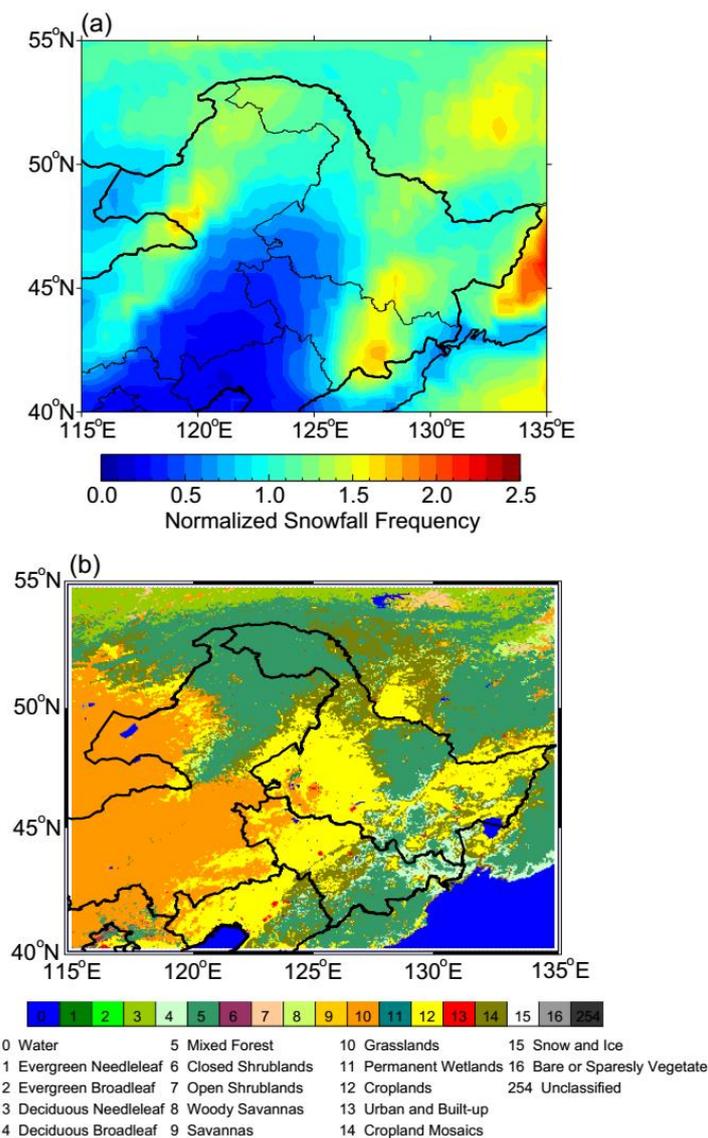
Figure 3. Spatial distribution of (a) the normalized snowfall frequency in January-February from 2003 to 2017 and (b) the different land cover types based on MODIS data in NEC.
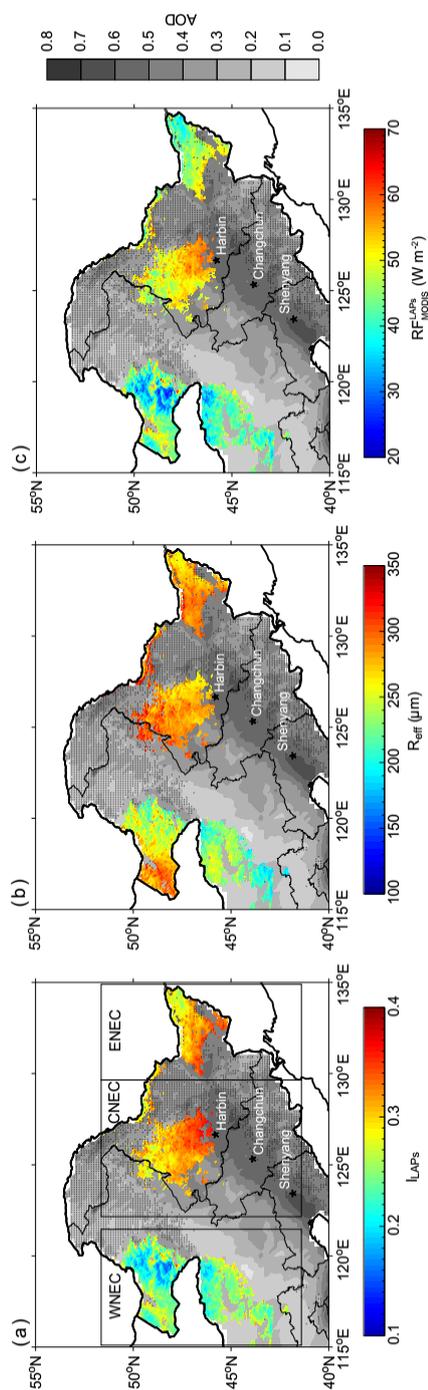
Figure 4. The spatial distributions of average (a) I_{LAPs}, (b) R_{eff}, and (c) RF_{MODIS}^{LAPs} in NEC in January-February from 2003-2017. The background shows the spatial distribution of MODIS AOD values. The dotted areas are covered by forests. The major cities in NEC are also shown in this figure. According to the geographical distribution, we separate the study area into three regions, western NEC (WNEC), central NEC (CNEC) and eastern NEC (ENEC).
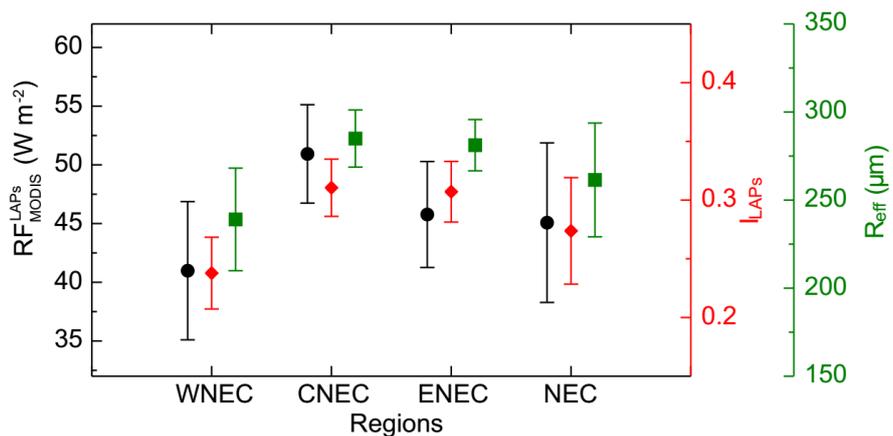
2 **Figure 5.** Statistics of average RF_{MODIS}^{LAPs}, I_{LAPs}, and R_{eff} in NEC in January-February

3 from 2003 to 2017.
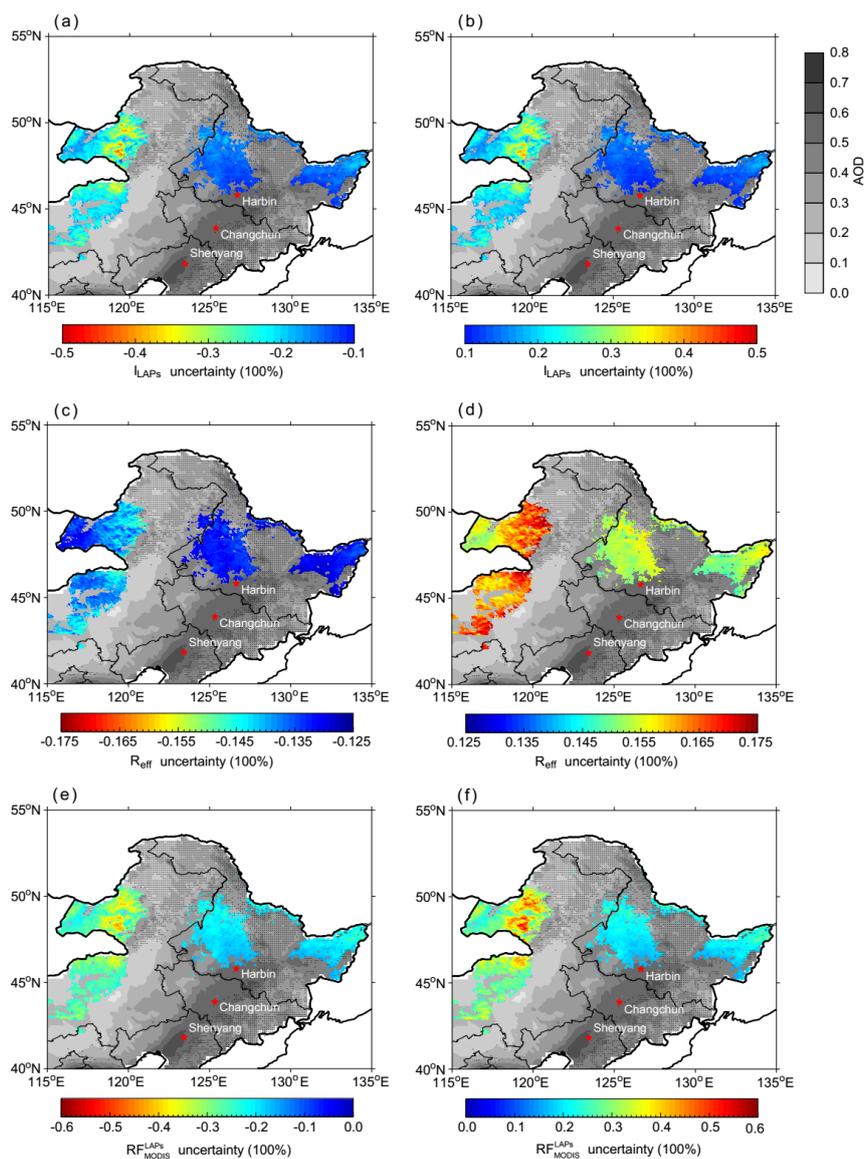
Figure 6. (a) Negative and (b) positive uncertainty of average I_{LAPs} in NEC in January-February from 2003 to 2017. (c) and (d) are similar to (a) and (b), but for R_{eff}. (e) and (f) are similar to (a) and (b), but for RF_{MODIS}^{LAPs}. The background shows the spatial distribution of MODIS AOD values. The dotted areas are covered by forests. The major cities in NEC are also shown in this figure.
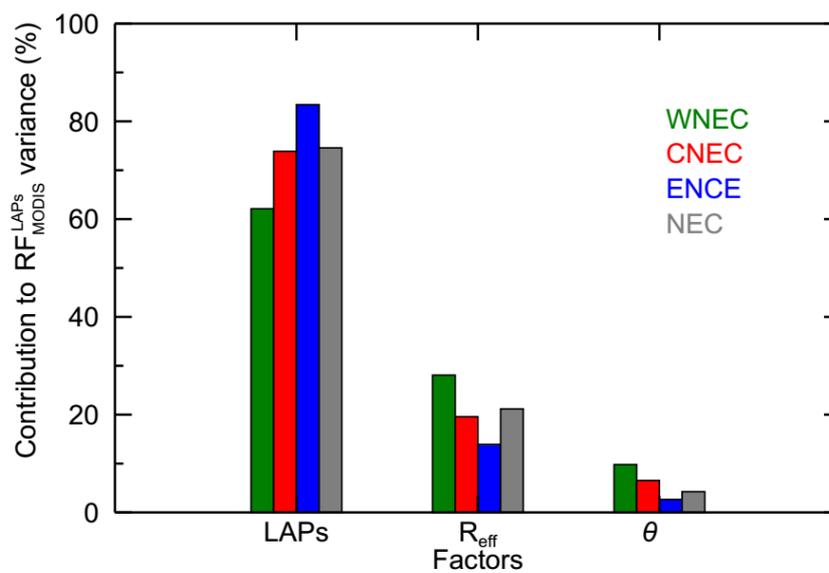
2 **Figure 7.** Fractional contribution of average I_{LAPs}, R_{eff}, and solar zenith angle (θ) to

3 the spatial variance of RF_{MODIS}^{LAPs} in January-February from 2003-2017.
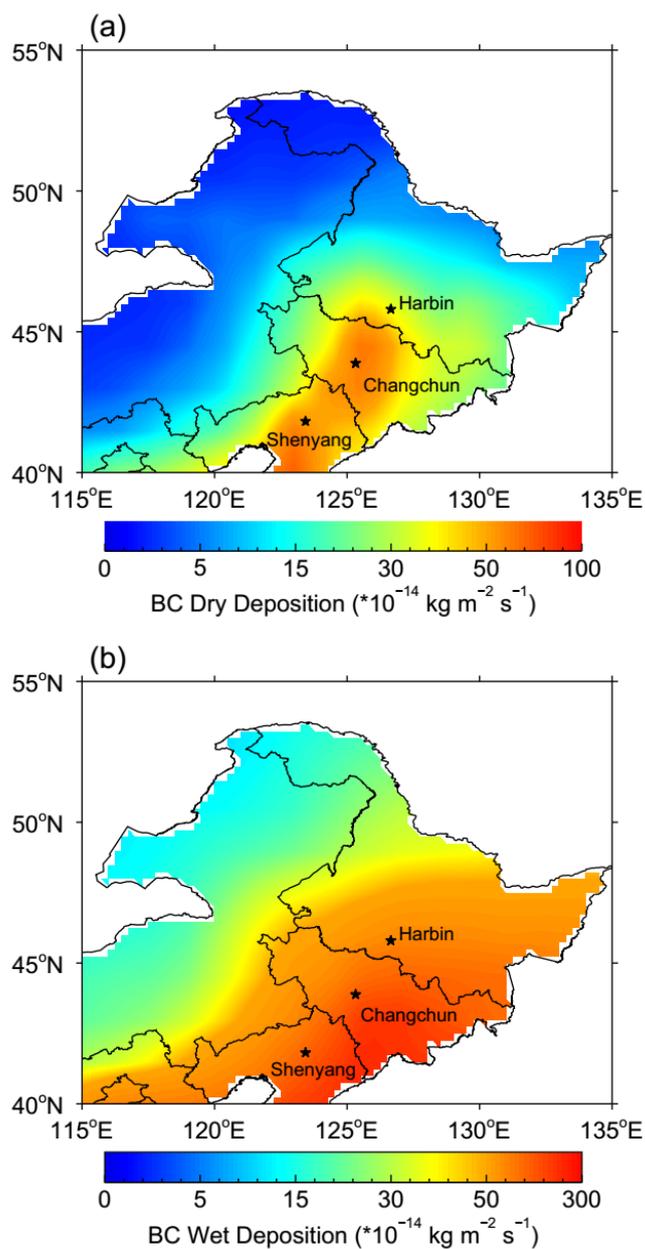
Figure 8. Spatial distribution of average (a) dry and (b) wet deposition of BC in NEC
in January-February from 2003 to 2005. BC deposition data is only updated to 2005.
The major cities in NEC are also shown in this figure.
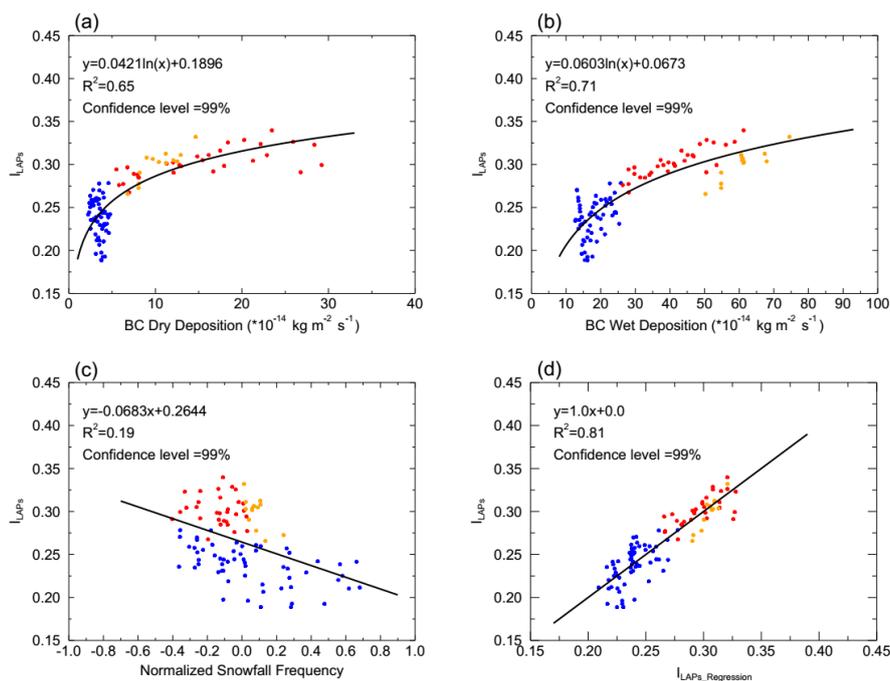
Figure 9. Scatterplots of (a) I_{LAPs} versus BC dry deposition, (b) I_{LAPs} versus BC wet

deposition, (c) I_{LAPs} versus normalized snowfall frequency, and (d) I_{LAPs} versus

regressed I_{LAPs} ($I_{LAPs\_Regression}$), which is regressed with BC dry and wet deposition

and snowfall frequency using multiple linear regression. We note that all data in this

figure is from January-February of 2003-2005 due to that BC deposition data is only

updated to 2005.
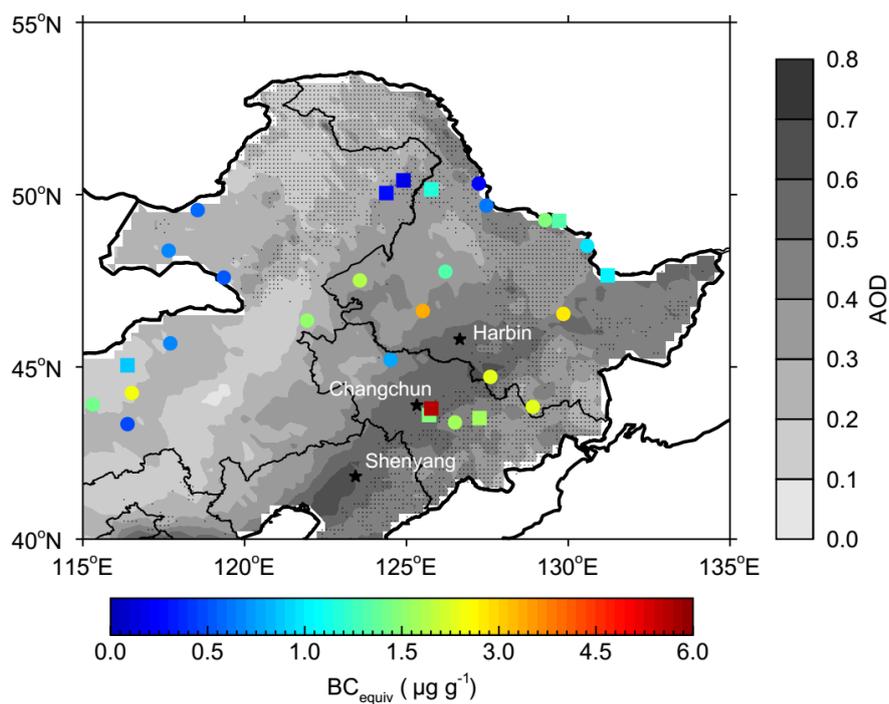
Figure 10. Spatial distribution of the measured BC_{equiv} concentration in surface snow
in NEC. Circles and squares represent the snow samples collected in 2010 (Wang et a.,
2013) and 2014 (Wang et a., 2017), respectively.
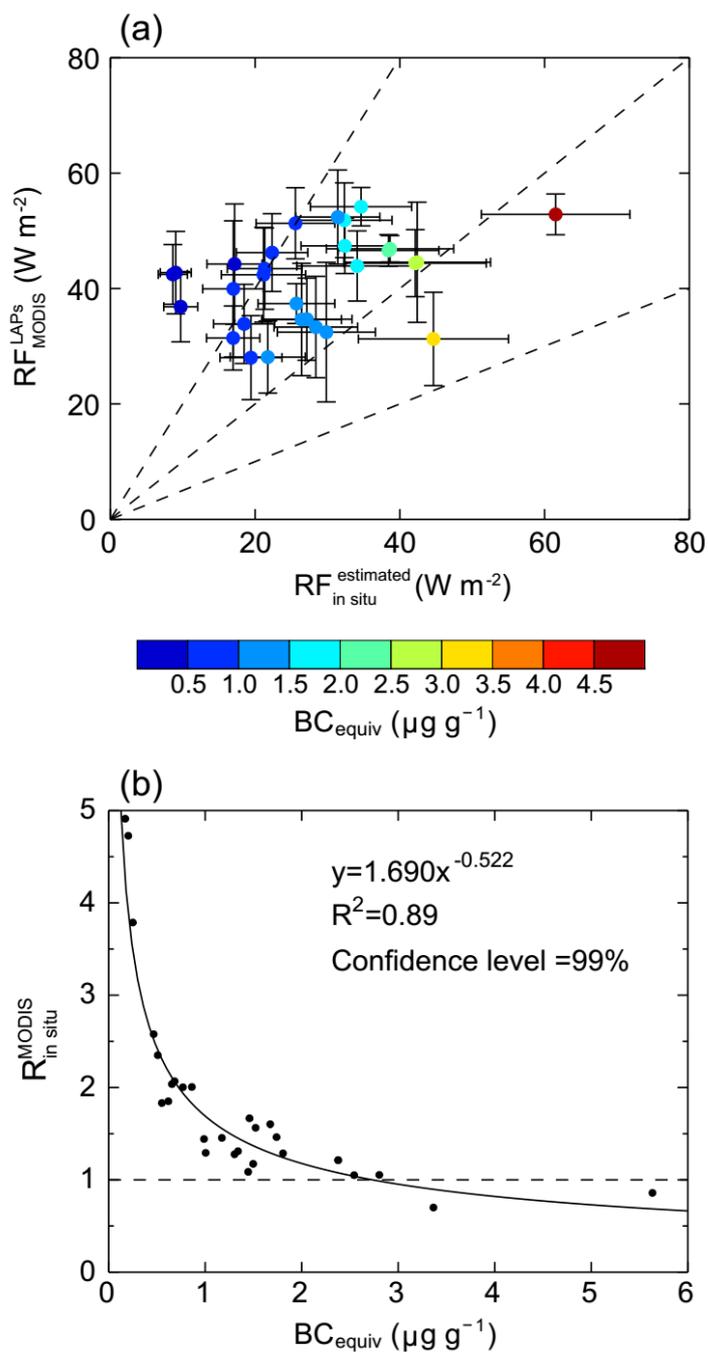
2   **Figure 11**. Scatterplots of (a) RF_{MODIS}^{LAPs} versus $RF_{in\ situ}^{estimated}$ and (b) $R_{in\ situ}^{MODIS}$ versus

3   BC_{equiv}.
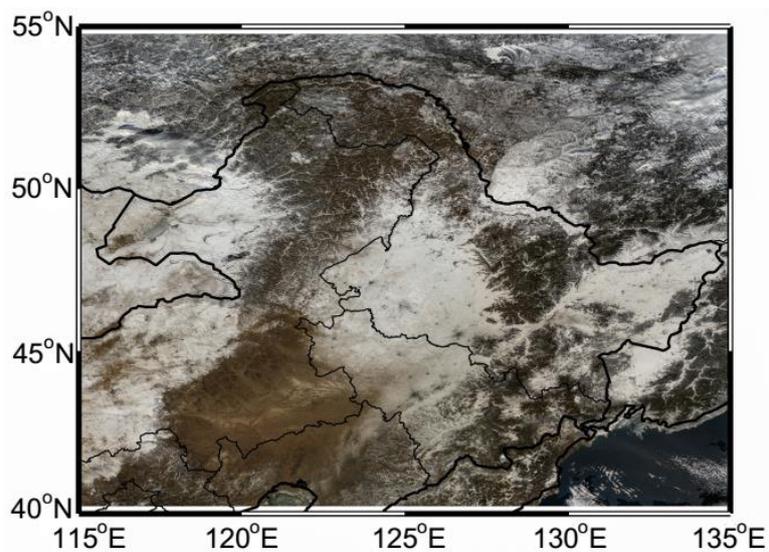
Figure 12. A true color map of MODIS in NEC at 23 January 2010.